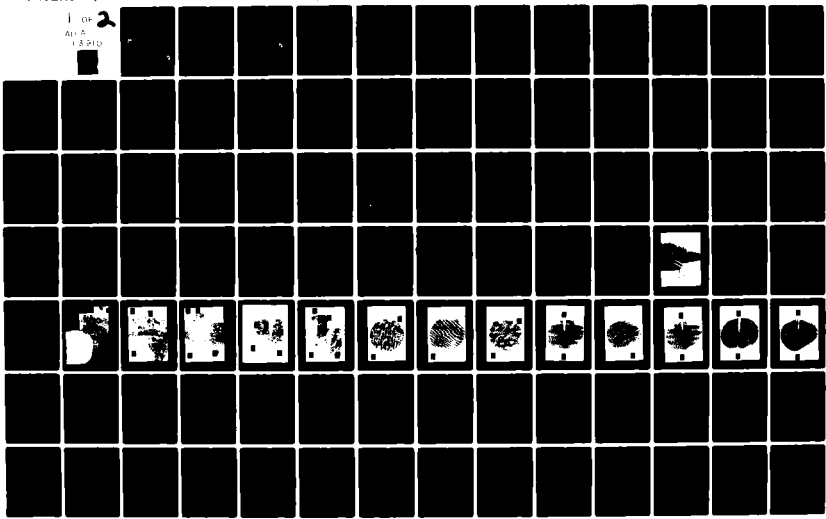


AD-A113 910 ROSE ENGINEERING AND RESEARCH INC INCLINE VILLAGE NV F/G 20/6
NEARFIELD AERODYNAMICS AND OPTICAL PROPAGATION CHARACTERISTICS --ETC(U)
FEB 82 W C ROSE, J E CRAIG, K R RAMAN F29601-79-C-0011
AFWL-TR-81-28 NL

UNCLASSIFIED

1 OF 2
AIAA
13 P10



AFWL-TR-81-28

AFWL-TR-
81-28

(2)

AU A 113910



NEARFIELD AERODYNAMICS AND OPTICAL PROPAGATION CHARACTERISTICS OF A LARGE-SCALE TURRET MODEL

William C. Rose, et al

Rose Engineering and Research, Inc.
Incline Village, Nevada 89450

February 1982

Final Report

Approved for public release; distribution unlimited.

AIR FORCE WEAPONS LABORATORY
Air Force Systems Command
Kirtland Air Force Base, NM 87117



82 04 27 025

This final report was prepared by Rose Engineering and Research Inc, Incline Village, Nevada, under Contract F29601-79-C-0011, Job Order 317J0201 with the Air Force Weapons Laboratory, Kirtland Air Force Base, New Mexico. Captain Richard K. deJonckheere (ARLB) was the Laboratory Project Officer-in-Charge.

When Government drawings, specifications, or other data are used for any purpose other than in connection with a definitely Government-related procurement, the United States Government incurs no responsibility or any obligation whatsoever. The fact that the Government may have formulated or in any way supplied the said drawings, specifications, or other data, is not to be regarded by implication or otherwise in any manner construed, as licensing the holder, or any other person or corporation; or as conveying any rights or permission to manufacture, use, or sell any patented invention that may in any way be related thereto.

This report has been authored by a contractor of the United States Government. Accordingly, the United States Government retains a nonexclusive, royalty-free license to publish or reproduce the material contained herein, or allow others to do so, for the United States Government purposes.

The Public Affairs Office has reviewed this report, and it is releasable to the National Technical Information Service, where it will be available to the general public, including foreign nationals.

If your address has changed, if you wish to be removed from our mailing list, or if your organization no longer employs the addressee, please notify AFWL/ARLB, Kirtland AFB, NM 87117 to help us maintain a current mailing list.

This technical report has been reviewed and is approved for publication.

Richard K de Jonckheere
RICHARD K. DEJONCKHEERE
Captain, USAF
Project Officer

Lawrence Sher
LAWRENCE SHER
Chief, Systems Development Branch

FOR THE COMMANDER

Demos T. Kyrazi
DEMONS T. KYRAZIS
Colonel, USAF
Chief, Laser Development Division

DO NOT RETURN COPIES OF THIS REPORT UNLESS CONTRACTUAL OBLIGATIONS OR NOTICE ON A SPECIFIC DOCUMENT REQUIRES THAT IT BE RETURNED.

UNCLASSIFIED

SECURITY CLASSIFICATION OF THIS PAGE (When Data Entered)

(Continued)

DD FORM 1 JAN 73 1473 EDITION OF 1 NOV 68 IS OBSOLETE

UNCLASSIFIED

SECURITY CLASSIFICATION OF THIS PAGE (When Data Entered)

~~UNCLASSIFIED~~

SECURITY CLASSIFICATION OF THIS PAGE(When Data Entered)

Block No. 20 (Continued)

Direct optical degradation information was obtained by holographic interferometry and quantified through techniques presented here. Aerodynamic measurements were made with hot-wire anemometry and multiple-port probes. Comparisons between the aerodynamically and optically deduced data are presented. These data can be used directly to estimate trends in expected loss of optical quality of a coherent beam for various flight speeds, altitudes, wavelengths and azimuthal turret angles. More data are now available for estimating the effects of unsteady aerodynamic flow fields on optical propagation quality. Data were obtained for Reynolds numbers near those occurring at full-scale flight conditions over a range of Mach number from 0.55 to 0.75. Investigation results generally agree with those obtained previously on smaller scale models and indicate that severe optical degradation can be present at aft-looking azimuth angles.

Accession For	<input checked="" type="checkbox"/>	<input type="checkbox"/>	<input type="checkbox"/>
REF ID:	DR&I	DR&C	DR&B
Justification	Reassessed		
Distribution/			
Availability Codes			
Dist	Avail and/or Special		



~~UNCLASSIFIED~~

SECURITY CLASSIFICATION OF THIS PAGE(When Data Entered)

SUMMARY

Direct measurements have been made of the aerodynamically induced optical degradation about a large-scale, on-gimbal laser turret and fairing combination typical of those proposed for use on large transport-class aircraft. The measurements were made in the turbulent flow field surrounding the turret with aerodynamic and holography instrumentation that allowed resolution of both the steady and unsteady fluid density fields. Sufficient aerodynamic data, including the levels and scale sizes of the unsteady density field, were obtained to allow calculation of the expected optical degradation caused by the turbulence. Holograms were quantified by procedures developed in the present study to allow estimates of both fluctuation levels and scales to be determined. Comparisons between results obtained with the two methods are presented. The data were obtained in a wind tunnel for Mach numbers between 0.55 and 0.75 for Reynolds numbers near those on full scale systems.

Data are presented in a form that can be used to estimate the trends in expected loss of optical quality of a coherent beam for various flight speeds, altitudes, wavelengths, and azimuthal turret angles. The present investigation extends the data base for aerodynamically induced optical degradation associated with the turret's near field.

Results of this investigation are in general agreement with those obtained previously on a smaller scale turret model. Trends in the data indicate that optical degradation increases substantially as azimuth angles increases toward the aft-looking positions. As shown here, this effect is quite pronounced at short wavelengths. Both temporal and spatial variations of wavefront distortions occurred over the aperture for certain conditions. A material window was tested at an azimuth angle of 60 deg and results indicate that wavefront distortion was reduced very little by the presence of the window.

PREFACE

Portions of the technical efforts were provided by Spectron Development Laboratories, Inc., Costa Mesa, California, under subcontract to Rose Engineering and Research, Inc. Additional technical efforts presented here were provided by Raman Aeronautics, Inc., Palo Alto, California, under contract to the National Aeronautics and Space Administration, Ames Research Center, Moffett Field, California.

CONTENTS

<u>SECTION</u>	<u>PAGE</u>
I INTRODUCTION	5
II WIND TUNNEL EXPERIMENT, INSTRUMENTATION AND ANALYSIS TECHNIQUES	8
III RESULTS AND DISCUSSION	24
IV CONCLUDING REMARKS	44
V RECOMMENDATIONS FOR FURTHER WORK	47
FIGURES	49
REFERENCES	93
ABBREVIATIONS AND SYMBOLS	95

I. INTRODUCTION

The propagation of coherent radiation through a gaseous turbulent flow medium can be adversely affected by the random variations of index of refraction and their spatial scales. In aerodynamic flows, the primary source of index changes is the unsteady fluid density field traversed by the radiation. These random variations result in wavefront aberrations that prevent a beam from being focused to its smallest spot size. Resulting aberrations are important in areas such as airborne astronomical observations, radiation sensing imagers, and the propagation of high-energy laser beams from airborne platforms to distant targets. Since these aberrations can be critical to some optical systems operations, it is important to understand the origins and nature of the unsteady density field. For aerodynamically induced density variations, wind tunnels and airborne systems provide an environment to test the effects of various configurations on the density field. Turbulent flows can be produced that represent portions of the flow field likely to be encountered or complete models of the hardware can be tested. Quantitative measurement of these flow fields is of utmost importance.

Recent Air Force Weapons Laboratory (AFWL) research programs have used extensive aerodynamic and optical instrumentation to quantify the optical effects of various turbulent flows. Correlation between directly observed optical quality and that calculated from measured aerodynamic quantities has been established (Refs. 1 and 2) so that optical quality may be assessed

even in flows that are essentially impossible to study optically. Past wind tunnel and flight experiments have been conducted in a cooperative program between the AFWL, the National Aeronautics and Space Administration's (NASA's) Ames Research Center and the Air Force Flight Dynamics Laboratory (AFFDL) to investigate aerodynamical-optical interactions. The program, known as the Aero-Optics Program, has been ongoing for the past 7 yr. Wind tunnel and flight experiments have been carried out under this program to study simplified two-dimensional components of the expected complex turbulent flow over a turret. Aerodynamic data were obtained in several representative turbulent flow fields to assess the effect of the unsteady density on the transmission of a coherent beam perpendicular to the plane of the flow. These studies examined attached boundary layers, shear layers generated by porous fences, and flows over open cavities. The reader unfamiliar with these studies is referred to the information presented in References 1 through 5. Results from these previous tests have indicated that the optical degradation due to planar, two-dimensional turbulent flows representative of those expected in laser propagation normal to the flow are relatively small for all but short wavelengths, typical of visible radiation.

These studies, however, did not consider the effects of looking through the full three-dimensional flow produced by a turret. A small scale coelostat type of turret and fairing combination was tested in a wind tunnel over a range of Mach numbers that included supersonic flow (Ref. 6). Measurements were made with hot-wire anemometry around the turret at azimuth

angles of 60, 90, 120 and 150 deg without the fairing and 60, 90 and 120 deg with the fairing present. Considerable increases in density fluctuation level and scale size were observed with increasing azimuth angle, producing strong optical phase aberrations at the larger angles. For the 90-deg case, optical losses were found to be higher than estimated on the basis of previous planar, two-dimensional aero-optical investigations because of the significant increase in local Mach number over the freestream Mach number. The addition of a fairing to the turret did little to aid in the optical quality, although fairings are known to be quite useful in reducing dynamic loads on the surface and within the optical cavity of the aperture.

The wind tunnel test described in this report was carried out as a part of the Aero-Optics Program (A-O V) to substantiate these results for a larger scale model that also allowed direct optical propagation data to be obtained.

II. WIND TUNNEL EXPERIMENT, INSTRUMENTATION AND ANALYSIS TECHNIQUES

A large (0.3) scale model of the U.S. Air Force Airborne Laser Laboratory's (USAF ALL) Cycle III turret and fairing was tested in the NASA-Ames 14-ft wind tunnel in the Fall of 1980. The model was mounted on a vertical splitter plate (Fig. 1) that effectively eliminated the tunnel sidewall boundary layer. This model and model support system have been used previously in several wind tunnel tests (e.g., Ref. 7). The turret is of the on-gimbal type and was tested with and without the aft fairing present. Turret specifications are described in detail in Reference 8. The radius of the cylinder and hemisphere is 21 cm. Aperture diameter is about 20 cm and was surrounded by a porous lip that projected about 2.5 cm out from the turret. All testing was done with the aperture open and porous lip on except for a few runs at an azimuth angle of 60 deg using a material window. Data were collected at freestream Mach numbers of 0.55, 0.65 and 0.75 to cover the range of expected flight Mach numbers. Since the Ames 14-ft wind tunnel is an open plenum tunnel, the Reynolds numbers changed with each change in Mach number as follows:

$$M = 0.55 ; Re/m = 9.5 \cdot 10^6$$

$$M = 0.65 ; Re/m = 10.6 \cdot 10^6$$

$$M = 0.75 ; Re/m = 11.2 \cdot 10^6$$

Figure 1 shows some important features of the model and test setup. The optical axis of the turret is shown at 90 deg azimuth and 0 deg elevation angles. Testing was carried out at

60, 90, 120 and 150 deg azimuth angles -- all for 0 deg elevation. A return mirror used in the direct propagation optical analysis is shown in the floor fairing at the bottom of the photograph. This return mirror could be positioned at 60, 90 and 120 deg. A section covered by retroreflective material (the light portion of the splitter plate) is shown that was used for the flow visualization optical analysis. The small forward fairing (left side of photograph) was present throughout the test. However, the aft fairing was used only for the 60 and 90 deg positions. The aerodynamic data were obtained using the dual probe drive assembly shown (Fig. 1) fastened to an extension plate between the splitter plate and the floor of the tunnel. The probe arms could accept either steady or unsteady aerodynamic instrumentation that could be traversed throughout the flow along a single line at the center of the optical path. The three azimuth angles of 90, 120 and 150 deg were surveyed with the one-dimensional drives by repositioning the entire probe drive assembly at each angle. The optical and aerodynamic instrumentation used to investigate the steady and unsteady density field around this turret model are discussed next.

Optical degradation produced by a turbulent flow can be measured quantitatively by classical optical techniques. However, in practice, these measurements are difficult because of vibration, optical component deformation, effects of extraneous degradation, and poor signal-to-noise ratios. Certain forms of laser holography can be used for this purpose that are less sensitive to some of these problems. Direct measurement of

optical wavefront distortion can be accomplished by interfering a plane optical wave with the distorted transmitted wave. The capability of holographic reconstruction of optical waves greatly simplifies practical aspects of interferometry where plane reference waves are interfered with by the distorted wave. Holographic interferometry is accomplished in vibration free environments by recording both the plane optical wave (flow-off) and the distorted optical wave (flow-on) on the same holographic plate. When reconstructed, such holograms reproduce both optical waves and, of course, the resulting interference depicts the flow-on wavefront distortion. The interference pattern is known as infinite fringe because when both waves are plane or undistorted, the resulting fringe spacing is infinite. If a small angle is introduced between the wavefronts, the fringe spacing becomes finite and the resulting interferogram is one having finite fringes.

A limited amount of vibration can be tolerated by recording the plane and distorted waves on separate holograms. In reconstruction the relative hologram positions are adjusted to achieve either the infinite or the finite fringe configuration. Quantitative data for the distribution of mean density about planar and axisymmetric bodies have been obtained (see Ref. 9, for examples and a complete description of this process). However, in high vibration environments the optical ray paths throughout the optical and flow components vary so significantly between the flow-on and flow-off pulses, that repositioning efforts during reconstruction are many times futile and, in general, these

double plate holograms are not practical.

An alternative technique has been developed for high vibration environments in which two holograms are recorded in rapid succession on a single plate. The two recordings are accomplished by double pulsing the laser, that is, the laser produces two short pulses (about 20 ns each) of light. The two pulses are separated in time, varying between 1 and 500 μ s. Since there is flow for each pulse, both pulses are transmitted through the distorting media, and in reconstruction the interference produced depicts the change in wavefront distortion between the two pulses. Hence, the technique is limited to dynamic events such as fluid mechanical turbulence.

Quantitative interpretation of the double-pulse holographic interferograms is complicated compared with that of the double plate holographic interferograms because the flow is on during both pulses. In conventional holographic interferometry, one well characterized pulse, usually plane, interferes with the object wave, and the resultant optical distortion is measured directly. In double pulse holographic interferometry neither pulse is well characterized. However, the fact that each pulse travels the same volume of turbulent flow is the basis for the quantitative interferometry analysis presented here.

Since the mean flow in which the turbulence is located is steady in time, the turbulence statistics such as velocity and density correlations are time invariant (i.e., the turbulence is stationary). Hence, for optical waves which traverse such media, the spatial statistics of the wavefront distortion or phase

fluctuation in space are also time invariant.

The relative phase shift, $\Delta\phi$, is the change in the wavefront distortion between the first and second pulses and is the phase shift that is measured from the reconstructions. Statistical quantities are determined only for the relative phase shift. The optical phase change due to turbulent flow fluctuation between pulses produces the fringe distortion which appears as noise on the otherwise straight finite fringe patterns. The amplitude of the phase distortion is scaled by the nominal fringe spacing. A relative phase or wavefront distortion of 2π rad or one wavelength, respectively, produces a deviation of one fringe spacing in the nominally straight fringes. An analysis is developed here that relates these measured statistics to those of the absolute phase shift, ϕ , actually present in the fluid. The basic assumption required for such analysis is that the phase statistics are stationary in space and time. The phase shift between pulses depends not only on the flow dynamics, but also on the pulse spacing, Δt .

For short time intervals in which no appreciable fluid motion occurs, the phase shift is everywhere very small or zero. Conversely, for long time intervals the amplitude and scale of the relative phase shift would become independent of the time interval. These two limiting time intervals can be estimated in terms of the phase statistics of the output wave. The time correlation function of the phase is

$$R_{\phi}(x, \Delta t) = \lim_{T \rightarrow \infty} \frac{1}{T} \int_{-\frac{T}{2}}^{\frac{T}{2}} \phi(x, t) \phi(x, t - \Delta t) dt \quad (1)$$

which is written here as

$$R_{\phi}(x, \Delta t) = \langle \phi(x, t) \phi(x, t - \Delta t) \rangle$$

Because the process is assumed to be spatially and temporally stationary, the time correlation is independent of the spatial position at which it's measured and the spatial correlation is independent of what time it's measured. Hence, the time correlation is written simply as

$$R_{\phi}(\Delta t) = \langle \phi(t) \phi(t - \Delta t) \rangle$$

The integral time scale is

$$\Lambda_{\phi, t} = \langle \phi^2(t) \rangle \int_0^{\infty} R_{\phi}(\Delta t) d(\Delta t) \quad (2)$$

Short and long pulse spacing are defined relative to the integral time scale $\Lambda_{\phi, t}$. For short pulse spacing, the phase shifts at the two times are correlated so the phase shift between pulses is small or zero, while for long pulse spacing, the phase shifts at the two times are uncorrelated. If there is no correlation, the phase shift between pulses, $\Delta\phi$, must be a random function with time correlation and scale which are independent of the pulse spacing Δt . Since the temporal statistics of the phase shift between pulses are independent of pulse spacing for all points in the turret aperture, the spatial statistics are also independent.

The spatial correlation of the phase shift between pulses is equivalent to the spatial correlation of the absolute phase shift when the pulse spacing is long compared to the integral time scale. The spatial correlation of the phase shift between pulses is

$$R_{\Delta\phi}(\Delta x) = \langle \Delta\phi(x-\Delta x) \Delta\phi(x) \rangle \quad (3)$$

which can be written in terms of the absolute phase shifts as:

$$\begin{aligned} R_{\Delta\phi}(\Delta x) &= \langle \phi_2(x) \phi_2(x-\Delta x) \rangle + \langle \phi_1(x) \phi_1(x-\Delta x) \rangle \\ &\quad - \langle \phi_1(x) \phi_2(x-\Delta x) \rangle - \langle \phi_2(x) \phi_1(x-\Delta x) \rangle \end{aligned} \quad (4)$$

where the subscripts 1 and 2 indicate the time for each pulse. Since the process is time stationary, the first two terms are equal and, in fact, are the spatial correlation of the absolute phase, i.e.:

$$\begin{aligned} R_{\Delta\phi}(\Delta x) &= 2R_{\phi}(\Delta x) - \langle \phi_1(x) \phi_2(x-\Delta x) \rangle \\ &\quad - \langle \phi_2(x) \phi_1(x-\Delta x) \rangle \end{aligned} \quad (5)$$

Before proceeding further with this analysis, some assumption about the statistics of the absolute phase is required. This is because the interferogram contains the results of the integrated effect of the turbulence along the beam path. It has been assumed, for simplicity, that the statistical parameters are homogeneous and isotropic. Notice that this is much less restrictive than to assume that the turbulence itself is homogeneous and isotropic. Under this assumption, the two cross-correlation terms in Equation 5 are equal for all pulse spacings, Δt . For very short pulse spacings (i.e., $\Delta t \ll \lambda_{\phi,t}$), ϕ_1 and ϕ_2 are highly correlated so that the two cross-correlation terms become equal in magnitude to $2R_{\phi}(\Delta x)$ and, thus, $R_{\Delta\phi}(x)=0$. However, for long pulse spacings, compared with the integral time scale of the turbulence (i.e., $\Delta t \gg \lambda_{\phi,t}$), ϕ_1 and ϕ_2 are uncorre-

lated and both of the cross-correlation terms are zero. As shown in Section III, integral time scales for the present flows are about 50 to 150 μ s, so the 400 μ s pulse spacing used in this study is, in fact, long with respect to those integral time scales. Therefore, the primary result of the analysis is that the spatial correlations of the relative and absolute phase shift differ only by a factor of two, i.e.:

$$R_{\Delta\phi}(\Delta x) = 2R_\phi(\Delta x) \quad (6)$$

Using Equation 6, one may completely quantify the double-pulsed laser interferometric holograms. For ease in data reduction, only the zero spatial offset case ($\Delta x = 0$) was considered here. This produces the phase variance directly as:

$$R_{\Delta\phi}(0) = \sigma_{\Delta\phi}^2 = 2\sigma_\phi^2 \quad (7)$$

Now recall that for the case of a double pass through the turbulence, the single pass variance can be found as

$$\sigma_\phi^2 | \text{single pass} = \frac{1}{4}\sigma_\phi^2 | \text{from double pass}$$

so that

$$\sigma_\phi^2 | \text{single pass} = \frac{1}{8}\sigma_{\Delta\phi}^2 | \text{from double pulsed hologram} \quad (8)$$

Equation 8 was used in the present study to quantify the propagation holograms of the unsteady index-of-refraction field present in the shear and boundary layers over the turret.

Two complete pulsed-laser holographic interferometry systems and a continuous-wave-laser wave-shearing interferometry system were used to observe turbulence in the test. The propagation optics, consisting of one holography system and the wave-shearing system, were used to provide diagnostic measurements and general flow visualization along the beam propagation path. The flow visualization optics, the other holography system, were used to visualize the flow over the turret and fairing. A general

installation schematic of the optical systems is shown in Figure 2.

The propagation optics were composed of two optical systems, and, with a small change of optics, each system could be directed through the turret and returned from a floor mounted mirror along its original path (Fig. 3). This system has been used and described previously in Reference 10. A Holobeam pulsed ruby laser was used for the light source in the holography system. An InRad Q-Switch with an Apollo power supply was used to double pulse the laser cavity with a 400- μ s time interval between pulses. A HeNe laser was passed through the ruby laser cavity and aligned so that the low power laser could be used for optical system alignment. The beam was spatially filtered and passed through a beam splitter. The reflected beam was collimated at a 10-cm diameter and used as the reference beam. The transmitted beam was collimated at a 15-cm diameter and passed into the turret as the object beam. The object beam was directed out through the turret aperture and down to the floor mirror and returned along its original path. This beam then was reflected from the beamsplitter and directed onto the hologram. The reference beam path length was matched to that of the object beam and then directed onto the hologram to overlap the object beam. Holograms were recorded on 4 x 5-in AGFA GEVAERT, 10E75 film at an approximate diameter of 5 cm.

The wave-shearing interferometer system used a high-speed movie camera and a 200 mW Lexel, argon-ion laser as the light source. The green line was selected from the output beam and

spatially filtered and passed along the same path as the object beam for the holography system. The return beam was recollimated at a 2-cm diameter after the beamsplitter and passed through a shear plate. The shear plate was oriented 45 deg to the beam path and the front and back surface reflections were directed into the Hycam high-speed camera. A 50-mm imaging lens was used to reduce the beam size and focus the turbulence. The camera was operated at two speeds (5,000 and 10,000 frames per second) to ensure adequate film exposure.

The flow visualization system used a pulsed Korad ruby laser as the light source for reflection holography (Fig. 4). A HeNe laser was directed through the ruby laser cavity and used for alignment. The beam was split and both the reference and object beams were spatially filtered. The reference beam was matched to the correct path length and collimated at an 8-cm diameter on the hologram. The object beam was directed onto a retroreflective material applied to the splitter plate model. The reflected light was collected with a 12-cm lens and focused in a plane about 20 cm behind the hologram. The holograms were recorded on 70-mm AGFA GEAVERT, 10E75, film which was loaded into a Hassabland film back. Wavefront distortion was recorded for Mach number 0.55, 0.65, and 0.75 and for turret angles of 60, 90 and 120 deg. The turret port configuration was open with the porous fence encircling the aperture for all three turret angles. A glass window was also used without the porous fence to examine the optical effect of flow penetration at the forward looking 60-deg turret angle. A yarn tuft grid was placed in the aperture plane for the open port 60-deg turret angle case and photographed with

the high-speed camera to investigate the unsteady flow within the cavity itself.

Both laser holography systems used ruby light at $0.69 \mu\text{m}$ wavelength. Data taken at this wavelength can be easily scaled to others by the well known scaling relationships (Ref. 2).

The quantitative procedure given for reducing the double pulsed hologram data is a very useful one. However, recall that the recorded wavefront information is one of an integrated nature along the entire optical path. To fully quantify any type of integrated optical measurement, some assumption about the statistics of the turbulence (as used above) or about the turbulence itself is required. In contrast, aerodynamic instrumentation can be used to make point measurements throughout the turbulent flow of the steady density field and both the fluctuation levels and correlation volumes of the unsteady density field, from which the integrated optical quality may be calculated (Refs. 3 or 6).

Aerodynamic instrumentation was chosen to measure the steady and unsteady flow properties at selected locations in the flow about the turret. Since this instrumentation must be positioned physically in the flow field, only a limited region of the flow can be realistically considered for measurement. For this optics-related test, the instrumentation was positioned along the centerline of the optical beam path. Two independently positionable probe drives allowed any pair of sensors to be placed anywhere along the radial path at azimuth angles of 90, 120 and 150 deg.

The basic steady flow measurements in the general three-

dimensional flow about the turret were made with a single, conical-tipped, five-hole pressure probe mounted to one of the probe drives. Extensive pretest calibrations over the range of expected Mach numbers and flow angles over the probe were carried out at the USAF Academy wind tunnel. The five pressures obtained in an unknown flow can be used in conjunction with the calibration curve fits to yield the local flow velocity vector relative to the probe axis and the local total pressure parameter. Flow direction angle and flow Mach number are directly output from the data reduction sequence. Since the test flow is adiabatic, the total temperature throughout the flow field is known and the velocity magnitudes, as well as the steady density and temperature fields, can be easily calculated. The calibration and data reduction procedures for the probe used here are similar to those used in Reference 4.

The unsteady flow measurements were made to assess the nature of the unsteady density field affecting the quality of optical propagation. No proven aerodynamic instrumentation is available for directly measuring the density fluctuation levels or their scales in the type of turbulent flows encountered in the present test. Point measurements of fluctuating static pressure, total temperature, and mass flux can be made and, through the complete analysis that follows can be combined to yield the fluctuating density. Static pressure measurements are generally difficult to accomplish. However, using the probes and techniques outlined in Reference 11, one can make useful measurements in the turbulent flow fields of the present test. Total tempera-

ture and mass flux fluctuations are made by an unheated and heated high response sensor, respectively. The procedures used here for calibration and use of hot-wire anemometry in transonic flows containing high turbulence have been given in detail elsewhere (e.g., Refs. 3, 5, 6 and 12). Comparisons between data obtained with a laser velocimeter and a hot-wire anemometer (Ref. 5) indicate that the data acquisition and analysis procedures used here remain valid in the regions of interest to optical propagation quality. In situ calibrations were used for each sensor used in order to minimize the uncertainty in the calibrated sensitivity. These sensors are 5 μm in diameter and are about 1 mm long. They were used in the flow with their axis parallel to the nominal two-dimensional plane of the shear layers to produce the best spatial resolution and virtually eliminate any effects of flow angularity over the probe. Overall uncertainty in the fluctuating parameters obtained with hot-wire anemometry can be expected to be about 10 percent. The directly obtained data can be converted to the desired density fluctuations through the following analysis, starting with a differential form of the equation of state

$$\frac{\rho'}{\bar{\rho}} = \frac{\rho'}{\bar{\rho}} + \frac{T'}{\bar{T}} \quad (9)$$

This can be combined with a differential form of the thermal energy relationship

$$T_t = T(1 + \frac{\gamma-1}{2} M^2)$$

i.e.

$$(1 + \frac{\gamma-1}{2} M^2) \frac{T_t'}{\bar{T}_t} = \frac{T'}{\bar{T}} + (\gamma-1)M^2 \frac{u'}{\bar{u}} \quad (10)$$

to give

$$(1 + \frac{\gamma-1}{2} M^2) \frac{T_t'}{\bar{T}_t} = \frac{p'}{\bar{p}} - \frac{\rho'}{\bar{\rho}} + (\gamma-1)M^2 \frac{u'}{\bar{u}} \quad (11)$$

Adding and subtracting $(\gamma-1)M^2 \frac{\rho'}{\bar{\rho}}$ on the right-hand side of equation gives

$$(1 + \frac{\gamma-1}{2} M^2) \frac{T_t'}{\bar{T}_t} = \frac{p'}{\bar{p}} - [1 + (\gamma-1)M^2] \frac{\rho'}{\bar{\rho}} + (\gamma-1)M^2 \frac{(\rho u)'}{\bar{\rho} \bar{u}} \quad (12)$$

Equation 12 now contains the desired density fluctuation and the measured fluctuating quantities of total temperature, T_t' , pressure, p' , and mass flux, $(\rho u)'$. As shown in previous Aero-Optics investigations (see Ref. 3), the contribution of total temperature fluctuations to those of density are negligible and may be dropped from Equation 12.

We then have

$$[1 + (\gamma-1)M^2] \frac{\rho'}{\bar{\rho}} = \frac{p'}{\bar{p}} + (\gamma-1)M^2 \frac{(\rho u)'}{\bar{\rho} \bar{u}} \quad (13)$$

or, for convenience

$$A \frac{\rho'}{\bar{\rho}} = \frac{p'}{\bar{p}} + B \frac{(\rho u)'}{\bar{\rho} \bar{u}} \quad (14)$$

Furthermore, because of phase lags and physical limitations, the measurements of mass flux and static pressure cannot be made simultaneously so that a time averaged form of Equation 14 is used, i.e.:

$$A^2 \frac{\overline{\rho'^2}}{\overline{\rho}^2} = \frac{\overline{p'^2}}{\overline{p}^2} + 2B R_{ppu} \frac{\langle (\rho u)' \rangle \langle p' \rangle}{\overline{\rho u} \overline{p}} + B^2 \frac{\overline{(\rho u)'^2}}{\overline{\rho u}^2} \quad (15)$$

Where R_{ppu} is the zero-phase-lag cross correlation coefficient between $(\rho u)'$ and p' . In previous Aero-Optics tests (Refs. 3, 4, and 6) extensive efforts to obtain R_{ppu} between surface pressure sensors, stream static pressure sensors, and shear layer mass flux measurements indicated a negligible correlation coefficient.

Under this condition

$$A^2 \frac{\overline{\rho'^2}}{\overline{\rho}^2} = \frac{\overline{p'^2}}{\overline{p}^2} + B^2 \frac{\overline{(\rho u)'^2}}{\overline{\rho u}^2} \quad (16)$$

Now, whether both pressure and mass flux fluctuations are important to optical propagation depends entirely upon the nature of these fluctuations. For example, if the pressure fluctuations were caused by plane pressure waves propagating through the flow, their effect would be to introduce an optical tilt, at most. However, most of the previously observed pressure fluctuations have been observed to be random in nature, although they typically have a much larger scale size than those for mass flux.

Because of this uncertainty in exactly how the pressure fluctuations influence optical propagation, previous Aero-Optics reports (Refs. 3 and 6) have ignored their contribution to the calculated density fluctuations. These values were stated to be a lower bound since any optically important pressure fluctuation would add to the magnitude of the density fluctuations.

Since the present flow field was large enough to allow the use of the unsteady pressure instrumentation on both probe supports, a complete set of fluctuating pressure data, including integral correlation lengths (scale sizes), was obtained at $\theta = 120$ and 150 deg. These data are presented in conjunction with the mass flux fluctuation data and discussed in light of Equation 16 and its optical implications.

III. RESULTS AND DISCUSSION

The basic aerodynamics of the flow over the turret is composed of a subsonic freestream, locally sonic regions on the forward side of the turret, boundary layer separation near the 90-deg azimuth angle, and an intense free shear layer separating the high speed edge flow from the wake region downstream of and behind the turret. The boundary layer separation extends up each side of the turret and merges on the hemisphere forming a U-shaped separation line. The free shear layer and certain other relevant features of the flow field can be made visible with the aid of the flow visualization holography system. Such visualization provides a picture of the turbulence structure, geometry and location, and allows improved interpretation of propagation holography as well as the aerodynamic data. A reconstructed interferogram has been superimposed on a photograph of the model and is shown in Figure 5. The interferogram fringes depict the large scale, low intensity turbulence in the free stream. The turbulence in the shear layer is of much smaller scale and exhibits a much stronger optical phase aberration. The region of flow downstream and directly behind the turret reveals a larger scale turbulence of much lower intensity than that of the shear layer. Recall that the way in which the flow visualization holography system is set up will exhibit the effects of two regions of turbulence; normal propagation through the shear layer off the hemisphere portion of the turret and subsequent propagation through the wake region. This interferogram strongly indicates that the

turbulence in the shear layer is of much higher intensity and of a smaller scale than the turbulence in the wake. This suggests that optical distortion occurs primarily in the shear layer and almost none occurs in the very low speed aerodynamic wake region.

The turret is shown in the 150-deg position (Fig. 5) and a portion of the probe support flange can be seen downstream of the interferogram. Separation occurs upstream of the fenced aperture engulfing the entire aperture in turbulent flow. To quantify some of the features of this low Mach number ($M = 0.55$) case, the interferogram is enlarged in Figure 6. The freestream portion of the interference pattern is easily identified by the large scale fringes with length scales of about 100 mm. The outer edge of the shear layer is clearly defined because it borders the free-stream flow. The large wavy structure of the shear layer edge has length scales of about 40 mm, while the turbulence within the shear layer has length scales of about 10 mm. The inner border of the shear layer is less visible because wake turbulence and the shear layer developing over the hemisphere exhibits only slightly larger length scales. The larger scale wake turbulence has a length scale of about 40 mm.

The intermediate Mach number interferogram ($M = 0.65$) is shown in Figure 7. Again the freestream turbulence is easily identified by large scale fringes, except for this Mach number, the length scale is reduced to about 70 mm. Unlike the lower Mach number case, the outer shear layer border is fairly straight and makes an approximately 10-deg angle with the freestream direction. The inner shear layer border is again less visible

than the outer border. The shear layer thickness is measured to be 71 mm at position A and 91 mm at position B. The turbulence within the shear layer appears rather uniformly distributed when compared to the low Mach number case, and the length scale is reduced to about 8 mm. The wake region exhibits the large scale turbulence of about 40 mm.

The high Mach number interferogram ($M = 0.75$) is shown in Figure 8. Again, the freestream region is easily identified by large scale fringes; except for this Mach number the length scale is markedly reduced to about 40 mm. A large probe strut obscures much of the outer shear layer border. The turbulence within the shear layer is quite intense and has a length scale of 8 mm. Since the inner shear layer border is smeared, the shear layer thickness cannot be accurately measured from these optical data. It is interesting to observe the lack of turbulence in a portion of the shear layer at position C. The wake turbulence exhibits a smaller length scale of about 30 mm; smaller than either of the previously discussed cases. A second interferogram is shown for the high Mach number case for the sole purpose of displaying a large scale event at position D (Fig. 9). This large scale turbulent structure has a cross stream or vertical dimension of about 100 mm. The record of such an event is striking evidence of both the spatial and temporal turbulence dynamics, implying that large fluctuations in beam propagation quality are likely to occur.

Table 1 summarizes the various characteristic length scales observed for each Mach number. Notice that, aside from the free-

stream turbulence length scale the others are nominally unaffected by Mach number.

TABLE 1. LENGTH SCALES OBTAINED FROM
OPTICAL DIAGNOSTICS

M	0.55	0.65	0.75
Freestream Turbulence Length Scales	100 mm	70 mm	40 mm
Shear Layer Turbulence Length Scale	10 mm	8 mm	8 mm
Wake Turbulence Scale	40 mm	40 mm	30 mm
Shear Layer Thickness	~80 mm	80 mm	80 mm

In this section, the optical analysis presented in Section II will be used to interpret the propagation interferometry data. The pulsed ruby laser beam was propagated from the turret aperture and directed to the floor mounted mirror, which was aligned to reflect the beam along its original path. The original plane optical wave was passed twice through the distorting turbulent media about the turret and holographically recorded in the distorted state. Turret angles of 60, 90 and 120 deg and flow Mach numbers of 0.55, 0.65, and 0.75 were investigated. In general, the aperture was open and encircled by a porous fence. In addition, a material window with the fence removed was used at 60 deg.

The holographic interferometry was accomplished by double pulsing the ruby laser at a 400 μ s pulse spacing. The resulting interferometric images were reconstructed and photographed at the plane of the turret aperture. The interferograms were printed full scale at the 150 mm beam diameter allowing direct observation of the spatial turbulence scales. The fringe

distortion across the interferogram was measured along two separate fringes. The measured fringe distortion varied significantly about the aperture even within a single interferogram. A large number of interferograms must be recorded and reduced to determine accurate temporal or spatial beam quality statistics. Wind tunnel time constraints did not allow the recording of such a large number of holograms, and hence the data sample exhibits an unusually large amount of scatter.

Low Mach number interferograms for the 60-deg turret position are shown in Figures 10a and b. For the open port case the tuft grid was in place and the tufts are easily observed. Recall that the mean fringe orientation is random between holograms and, in general, does not line up with the indicated flow direction. The fringe distortion exhibits a much larger spatial variation for the open port case, where the fringe distortion in the cross stream sides of the aperture are larger than those in the center. For this specific case, the windowed aperture is of higher optical quality, although variation for shot to shot is of the same order as the difference with and without the window.

The intermediate Mach number data ($M = 0.65$) are shown for all three turret angles in Figures 11a, b, and c. Again for the 60-deg turret angle, the fringe distortion is worse in the cross stream edges of the aperture than the center. Fringe distortions of about one wavelength are measured in the aperture edge while in the aperture center the level is reduced to about $\lambda/3$. The length scale of the large amplitude distortion is about half the diagnostic beam diameter or about 75 mm. A similar result is

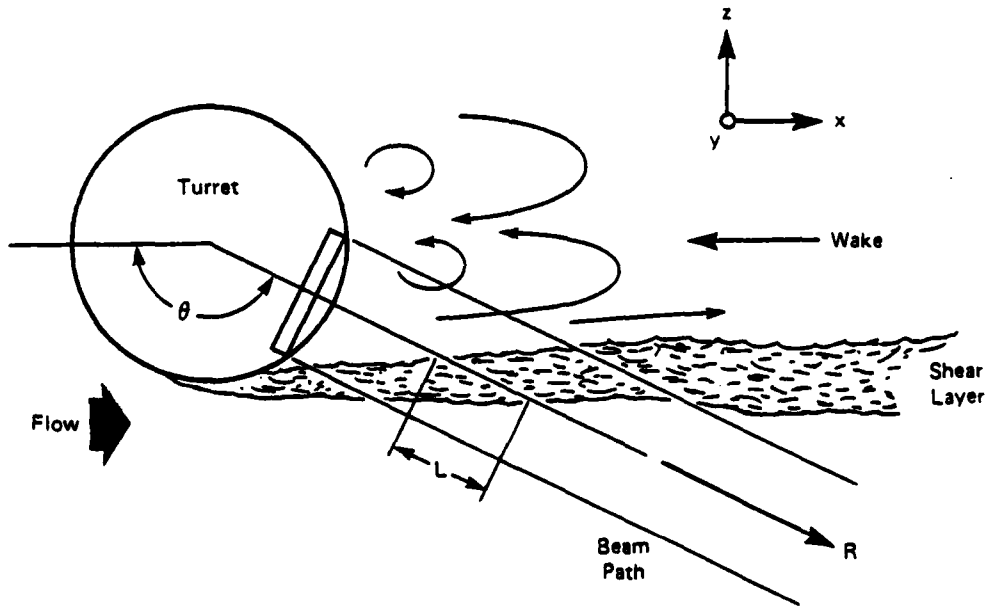
observed for the 90-deg turret angle, where 1.8 wavelength fringe distortions are observed in the aperture edge and 0.4 wavelength fringe distortions are observed in the aperture center. Again the large amplitude distortions have a length scale about 75 mm. A much smaller scale distortion of about 10 mm is also observed. The 120-deg turret angle interferogram was recorded with very little tilt between the pulses. The fringe distortion is more uniform (about 1.2 wavelengths) over the aperture for this turret angle.

Further quantification of the effect of turret azimuth angle is discussed with the aid of Figure 12. The 90-deg angle interferograms are shown in Figures 12a, b, and c for all three Mach numbers. The hot-wire probes are visible in the 0.55 and 0.65 Mach number cases, and the five-hole pressure probe is visible in the 0.75 Mach number case. The dominant effect of the cross-stream variation is observed in all cases. For the low Mach number case, the fringe distortion varies from 0.5 wavelengths in the aperture center to nearly 1.0 wavelength in the cross-stream edges. For the intermediate Mach number case, the fringe distortion varies from 0.8 wavelengths in the aperture center to 1.8 in the cross-stream edges. For the high Mach number case, the fringe distortion varies from as little as 0.5 wavelengths in the aperture center to almost 2.0 wavelengths in the cross-stream edges. This rather substantial variation of distortion across the aperture was not observed at the 120-deg azimuth angle. One possible explanation for the 90-deg spatial variation is that it is due to the turbulent flow streaming from the porous lip. Since at

120 deg this lip is submerged in the separation region, high turbulence would not be generated by it.

The propagation holograms shown here were selected to reveal the general nature of the optical distortion over the aperture for various flow conditions. More complete data have been reconstructed and quantified as to wavefront distortion. These data are presented in a later portion of this section in conjunction with the aerodynamically deduced distortion values.

The aerodynamic data are presented next with the steady, or mean, flow data being discussed first, then the fluctuating flow data. As an aid to understanding the coordinate system used in the presentation of these data, the following sketch is presented that shows the fixed coordinates, x and y, and the radial coordinate, R.



Steady flow data are important to the present study because they reveal the general nature of the flow in which the fluctuating index-of-refraction field is found. These data are required for full interpretation of the data acquired through hot-wire anemometry. The relevant steady-flow data for this test are the Mach number and mean density values and are shown in Figures 13 and 14 for all three of the test freestream Mach numbers. These data, as were all of the aerodynamic data presented, were obtained along a radial direction at the center of the optical path for the three azimuth angles indicated on the figures. Both the Mach number and density, $\bar{\rho}/\rho_\infty$, variations indicate that, at 90 deg the shear layers are very thin with large gradients. At 120 deg the layers are thicker, while at 150 deg their radial extent has increased to about 15 cm for all Mach numbers. This increase in radial extent of the shear layers is an important optical factor, since it is precisely this thickness that defines the optical path length, L, through the turbulence. As expected for the flow around the bluff turret, local Mach numbers at the edge of the shear layers are up to 25 percent higher than the freestream value. The mean density data indicate a variation through the shear layers that ranges from about 8 percent at $M = 0.55$ to about 20 percent at $M = 0.75$. These density variations arise as a result of the static temperature variations resulting from the changes in Mach number for constant total temperature through the shear layers. Of course, the observed density gradients can be viewed as the aerodynamic potential for the fluctuating density. In fact, if the scales of the turbulence were known throughout

these layers, the magnitude of the density fluctuations could be determined.

The unsteady aerodynamics data were obtained primarily to assess the optical quality of a beam propagated from the turret. The analytical relationship between aerodynamic data and optical properties, such as phase variance, σ^2 is well known (see Refs. 1, 2, 3, or 6, for example). Certain relevant portions of the complete analysis given in Reference 6 are given here to attempt to relate the aerodynamic and optical data. Previous investigations have shown that the phase variance, σ_ϕ^2 , due to the random index of refraction variations, is best represented by a term involving the density fluctuation and an exponential correlation function along the beam path:

$$\sigma_\phi^2 = \beta^2 \int_0^L \int_{-r}^{L-r} \overline{\rho'^2}(r) \exp\left(-\frac{|\Delta r|}{l_r}\right) d(\Delta r) dr \quad (17)$$

When the value of the correlation length l_r is small compared to the total path length L, then Equation 17 can be written as:

$$\sigma_\phi^2 = 2\beta^2 \int_0^L \overline{\rho'^2}(r) l_r dr \quad (18)$$

Equation 18 is convenient to use in practical calculations using the experimentally determined aerodynamic data. However, when the value of l_r becomes a significant percentage of L, Equation 18 will no longer be sufficiently accurate, and Equation 17 should be used to calculate σ_ϕ^2 . In the study of Reference 6, it was shown that Equation 18 produces a larger σ_ϕ^2 than Equation 17. Thus, from an optics viewpoint, Equation 18 yields a phase

variance that is pessimistic. The percentage error in the calculated σ_{ϕ}^2 using Equation 18 is about equal to the percentage value of ℓ_r/L . The σ_{ϕ}^2 from Equation 18 is exactly the σ_{ϕ}^2 that can be derived from the holographic data in Equation 8. We see from Equation 18 that if one can determine, from aerodynamic data alone, the values of $\overline{\rho'^2}(r)$, ℓ_r and L , then σ_{ϕ}^2 is readily calculable. These parameters can be obtained aerodynamically as shown in previous Aero-Optical investigations and were determined in this study, as well. Equation 18 also reveals the fact that, with optical data (i.e., σ_{ϕ}^2) determined from a single integrated path length through a region of turbulence, it is essentially impossible to determine the pointwise values of $\overline{\rho'^2}(r)$ and ℓ_r over the path L . At best only an average $\overline{\rho'^2}$ could be obtained, if L and ℓ_r were known. As shown in Reference 6, the cross-aperture scales ℓ_x and ℓ_y can also be important in calculating the focal plane intensity pattern of a propagated beam, particularly if they are of the same order as the size of the aperture.

In this study, aerodynamic data were obtained that allowed $\overline{\rho'^2}(r)$, ℓ_r , ℓ_x , and L to be explicitly determined for all the test cases. These data, along with other relevant data obtained from the unsteady flow field are presented below.

The velocity and density fluctuations shown in Figures 15, 16 and 17 were determined directly from the measured mass fluctuations by the techniques outlined in SECTION II (Eqs. 11 and 12 for example). The measured static pressure fluctuations are shown in Figure 18. Fluctuating pressures indicating large values of p'/p_{∞} in the shear layer regions are probably caused

by fluctuations in local stream angle on the probe rather than bonafide fluctuations in fluid pressure. However, in the wake regions the indicated static pressure fluctuations are much more reliable and indicate a level of about 1 to 2 percent of the freestream pressure for all Mach numbers. The mass flux fluctuation data were reduced to velocity and density fluctuations under the assumption that the mass flux fluctuations arise solely as a result of vorticity in the shear layers (i.e., by using Eq. 15 and neglecting the p' term). This technique gives a lower bound for the magnitude of the density fluctuations. The optical implications of analyzing the data with this method are discussed later in conjunction with the discussions of scale lengths of the various fluctuation terms.

Velocity fluctuations are shown in Figure 15 for the conditions tested here as a function of distance along the turret radius. The values of $\langle u' \rangle / \bar{u}$ in the wake region are very large. For values above about 40 percent, only qualitative interpretation is justified since the anemometry system underestimates fluctuations above that level. Turbulence values of u' / \bar{u} in separated regions of 100 percent are not uncommon; however, the important parameter from an optical point of view is that the absolute velocity fluctuations are low compared with the local speed of sound. Thus, these velocity fluctuations are essentially incompressible and cannot produce substantial density fluctuations, even though the turbulence level is extremely high.

Density fluctuations, $\langle \rho' \rangle / \bar{\rho}$ are shown in Figure 16 and indicate magnitudes of from 2 to 4 percent of the local mean

value. Since the mean changes through these shear layers, a form for presenting density fluctuations better suited to extrapolating the data to other conditions is given as $\langle \rho' \rangle / \rho_\infty$ in Figure 17. These data indicated a thin shear layer at the 90-deg azimuth angle. At 120 deg it had grown thicker, and, at 150 deg, it had grown so large that the limits of the probe drive prevented the outer region of the layer to be measured. Locations and qualitative behavior of the shear layers as evidenced by both the unsteady density data and the steady flow data are in agreement. One other presentation of the rms density fluctuation data is shown in Figure 19 as $\langle \rho' \rangle$ in kg/m^3 . This form is directly usable for the optical calculations such as Equation 18.

The total optical path length, L appearing in Equation 18 can be obtained in several ways. It is usually defined as the length of the beam path through nonzero turbulence regions. From this, Figures 17 or 19 are used to determine L. The shearlayer radial extent observed in Figures 13 and 14 are in agreement with those obtained from the density fluctuation data and are shown in Figure 20 denoted by Aero. Also shown in Figure 20 are those values of L obtained directly from the flow visualization holography data given in Table 1 as modified by the specific azimuth angle. Data are given for the three Mach numbers tested. There is no observed change in L from the optical data with Mach number. The aerodynamic data shows no first order change either, and the data from both techniques are in good agreement.

In addition, optical calculations and general quantification of the unsteady flow require information on the scale sizes

of the turbulence. Data for these scale sizes (defined as the integral scale of the turbulence) were obtained with both hot-wire anemometry and with static pressure probes. Using the two independently positionable probe drives, the scale sizes, λ_r , were determined for a direction along the beam path at each of the azimuth angles. Both the streamwise integral scale and the integral time scale (discussed with reference to holographic pulse spacing in Section II) were determined by using the time autocorrelation functions and the mean flow data.

Values of the optical axis direction scale lengths, λ_r , determined from mass flux and optical data are shown in Figure 21. The correlation lengths for pressure fluctuations obtained within the shear layers were up to twice those determined by the mass flux data. Since the measured pressure fluctuations in the shear layers are probably associated with flow direction changes over the probe, the indicated scale sizes would be a measure of those due to the general, low frequency (200 to 300 Hz) unsteadiness of the entire wake flow rather than the small scale, high frequency (up to 10 kHz) exhibited by the mass flux data. Within the wake region itself where the pressure probes are believed to accurately measure the fluctuations, the scales indicated are very large -- up to about the size of the aperture diameter. This is completely consistent with the expected unorganized shedding from the bluff turret. Although the pressure fluctuation levels are between 1 and 2 percent of the freestream pressure in the wake and the implied density fluctuations due to these pressure fluctuations would be at least 1 to 2 percent of

ρ_∞ , the large scales introduce primarily optical tilt, if they have any optical influence at all. The flow visualization holography data indicate that, in fact, the wake is optically quiescent. The large scale pressure fluctuations present in the wake appear to give rise only to large scale disturbances that could be corrected by state-of-the-art adaptable optics systems. These fluctuations, however, might have a rather large influence on the jitter experienced within the optics train in the turret since the pressure fluctuation scales are quite large. Loads produced by these fluctuations could be significant at larger azimuth angles when the entire aperture is submerged in the wake.

Returning to Figure 21, the lengths given are the average values of l_r through the shear layers. In striking contrast to the good agreement shown between optical and aerodynamic data for optical path length, there is a large discrepancy between the two techniques. The values deduced from the flow visualization holography (Table 1) do not change substantially with Mach number nor do they appear to increase as the shear layer grows in the downstream direction. The scale size growth as the free shear layer develops is well known property and has been observed in previous Aero-Optics tests (e.g., Ref. 6). Why the holography data do not indicate this clearly is unknown, although it might be that the optical data show primarily the smaller scales that are strong enough to cause wave distortion, while the aerodynamic data are derived as a mathematical property of the entire spectrum of the turbulent motions. To proceed, it must be assumed that the aerodynamically deduced scale lengths are the correct ones to use in

Equation 18 to obtain σ_{ϕ}^2 from the remaining aerodynamic data.

By using the values for $\langle \rho' \rangle$ from Figure 19, the scale lengths from Figure 21, and the total path length from Figure 20, the optical phase distortions given in Table 2 can be calculated.

TABLE 2. OPTICAL PHASE VARIANCE FROM
AERODYNAMIC DATA

M	$\sigma_{\phi}^2, m^2, \text{Aerodynamic } \cdot 10^{14}$		
	90 deg	120 deg	150 deg
0.55	0.96	4.7	29.8
0.65	1.3	9.7	24.3
0.75	2.5	14.8	68.7

These values of σ_{ϕ}^2 can be used to calculate the rms wave distortion, i.e., σ/λ for any wave length; and, in particular, can be used to calculate the distortion for $\lambda = 0.69$ m used in the optical propagation holography. These calculated distortions are shown in Figure 22 along with the values of σ/λ obtained directly from the propagation holograms and Equation 8. The optical data shown are the averages of the distortion across the aperture for several cases. At 90 deg there is a substantial variation of distortion over the aperture. For the $M = 0.65$ case the extremes as well as the average value are shown to indicate how large this spatial variation can be. The averages shown at 120 deg are representative of the entire aperture. Agreement between these optically deduced distortions and those

deduced from aerodynamic data alone is quite good, particularly at the 120-deg azimuth angle. Agreement is seen at this angle for not only the correct magnitudes but the trend of increasing distortion with Mach number is exhibited by both techniques. At the 90-deg angle there is general agreement with the two techniques, although the cross-aperture spatial variation could easily account for any disagreement. This is particularly true since the aerodynamic data were obtained only along the centerline of the aperture. In general, the observed agreement in Figure 22 lends credence to the quantitative procedures used for both the optical data reduction presented here and the aerodynamic data reduction as used throughout the Aero-Optics studies.

Behavior of the wavefront distortion, σ/λ , or the phase variance, σ_ϕ^2 , is of interest to flow diagnostics and optical propagation; however, in projecting high-energy laser beams from an airborne platform to a distant target, the energy actually striking the target is of primary interest. The effectiveness of the laser in producing target heating is dependent on not only the total power striking it, but on the area over which the energy is concentrated; i.e., the on-target intensity. If there were no phase aberrations in the complete path traversed by the beam, the intensity distribution in the focal plane (the target) would be the so-called "diffraction-limited" value. Because of many sources of aberrations, the focal plane peak intensity is decreased and the beam power is focused to a larger spot than the diffraction-limited value. The ratio of the actual focal plane peak

intensity to that which would occur in the diffraction limited case is known as the Strehl ratio and is used as a convenient, single number representation of severity of the phase distortions along the beam path. As shown in References 6, 13 and 14, when the cross-aperture scales ℓ_x and ℓ_y are small when compared to the aperture, a simple expression for the Strehl ratio is valid, i.e.:

$$\frac{I}{I_0} = e^{-k^2 \sigma_\phi^2} \quad (19)$$

Thus if these scales are small, the intensity ratio can be directly calculated once σ_ϕ^2 is known. In this test, measurements of ℓ_x were made directly with the hot-wire anemometry system by obtaining the integral time scale, $\Lambda_{\phi,t}$ from the time autocorrelation function and then using the mean flow velocity data to obtain the length scale as:

$$\ell_x = 0.8 \bar{u} \Lambda_{\phi,t} \quad (20)$$

Average values for the integral time scales observed in the shear layers at the various test conditions are given in Table 3.

TABLE 3. INTEGRAL TIME SCALES FROM AERODYNAMIC DATA

M	$\Lambda_{\phi,t}$, μs		
	90 deg	120 deg	150 deg
0.55	90	100	160
0.65	95	110	150
0.75	80	90	180

These average integral time scale values were used in Equation 20 to determine the values of ℓ_x shown in Figure 23. At the 90-deg angle, the values of ℓ_x are between four and five times those for ℓ_r -- a situation characteristic of newly generated shear layers. In contrast, at 150 deg the values of ℓ_x and ℓ_r are nearly identical, indicating that the shear layer is fully developed. This general behavior of the shear-layer length scales is precisely that which was observed in the small-scale coelostat model study reported in Reference 6. The values of ℓ_x range between about 3 and 7 cm and correspond to about 15 and 35 percent of the aperture diameter. Under these conditions, Equation 19 remains very useful for estimating I/I_0 .

Strehl ratios for the wind tunnel conditions are given in Figure 24 for four representative wavelengths calculated on the basis of the aerodynamically deduced σ_ϕ^2 . Note that the σ/λ values from Figure 22 could also have been used in Equation 19 to calculate I/I_0 and produced nearly the same results for the 90 and 120-deg angles for which these optical data are available. The general behavior of decreasing focal-plane intensity with increasing azimuth angle and decreasing wavelength is similar to that expected on the basis of the previous small-scale study of Reference 6. Decreases in Strehl ratio with increasing Mach number reflect the increase in σ_ϕ^2 values with Mach number given in Table 2. As is evident for short wavelength systems, aft looking propagation will be seriously degraded because of the turbulent shear layers. It is of interest to note that, although these data were acquired in a wind tunnel and not on full scale flight

hardware, in the $M = 0.55$ case, for example, the tunnel conditions correspond to a flight level of about 3 km. Thus the results of Figure 24a could be considered to be directly applicable to a low level mission involving an on-gimbal turret of 40-cm diameter. Extrapolation of these data to other flight conditions can be carried out under some reasonable assumptions. An example is presented that corresponds to a turret three times the diameter of the wind tunnel model. A flight level of 11 km at $M = 0.75$ is used. The $M = 0.75$ data are considered applicable, although the scaling of the l_r and L values in Equation 18 is not clearly evident at present. The flight Reynolds number based on turret diameter Re_D , flight would be about $6.7 \cdot 10^6$ while the wind tunnel data were taken at Re_D , wind tunnel $= 4.5 \cdot 10^6$. Although not the same numbers, they are both relatively large from the standpoint of turbulence shear layer behavior. A scaling involving a four-fifths power law could be used, although, the justification for it is not clear when both turbulence and cylinder wake flows are present. Thus, for ease in engineering estimation, the data for total path length and integral scale are simply scaled up linearly with turret diameter ratio -- i.e., a factor of 3 on each term. The density fluctuation level is scaled down by a factor of 0.16 due to the decrease in density with altitude. The overall scaling factor on σ_ϕ^2 is then 1.44 times that observed in the wind tunnel. The resulting Strehl ratios are given graphically as a function of azimuth angle in Figure 25. This extrapolation of the wind tunnel data indicates that short wavelength systems would suffer serious loss of power on target if they were to be used.

at aft looking angles.

IV. CONCLUDING REMARKS

A wind tunnel test was made on a large-scale laser propagation turret to assess the optical degradation suffered by a coherent beam passing through the turret's nearfield turbulence. Both steady and unsteady data were obtained in the shear layers and separation zones resulting from the flow over the turret at Mach numbers of 0.55, 0.65, and 0.75. Direct propagation laser diagnostics indicated that wavefront distortions were present at a 60-deg azimuth angle and became worse as that angle was increased to 120 deg. The direct optics data were supported by a complete set of aerodynamic, fluctuating-flow data, including magnitude of the unsteady density and its relevant scale sizes. Peak density fluctuation levels remained about the same as the azimuth angle increased from 90 to 150 deg, but increased slightly with increasing Mach number. However, both the scale sizes and total optical path increased substantially as azimuth angle increased. This resulted in a calculated value of phase variance that changed nearly two orders of magnitude over the full range of azimuth angles tested. This calculated wavefront distortion was compared with that obtained from the optical propagation diagnostics and very good agreement was shown between the two independent techniques.

The aerodynamic measurements were made along a single path in the flow that allowed resolution of the temporal characteristics but not the spatial variations of wavefront distortion over the entire aperture. Temporal variations of the turbulence

pattern indicate that about 10 percent of the time very good optical transmission could be expected, even for short wavelengths, although the time averaged wavefront would be severely degraded. The optical measurements, in contrast, clearly indicate the spatial variation of the wavefront distortion over the aperture at selected instants of time. It was shown that large spatial variations occurred for all Mach numbers for the 90-deg azimuth angle and almost none were observed when the aperture became submerged in the wake at 120 deg. Propagation optical data further indicated that, for the 60-deg azimuth angle where a material window was tested, the addition of the window did little to reduce the observed wavefront distortion.

Flow visualization holographic interferometry was also used in this test and revealed that the optical wavefront distortion occurs primarily in the free shear layer for turret angles beyond 90 deg. The turbulence in the wake region downstream of the turret was observed to have a much lower intensity than that observed in the shear layer. The fringe distortion observed in the wake region results primarily from normal propagation through the free shear layer developing downstream of separation from the hemispherical portion of the turret. The aerodynamic data fully support this finding as evidenced by the narrow band of high level density fluctuations found in the shear layers.

Phase variances found in this study were used to calculate the focal-plane intensity ratio for the wind tunnel conditions for various radiation wavelengths. It was shown that this ratio decreased rapidly with increasing azimuth angle and Mach number

while it decreased with decreasing wavelength. Because the aerodynamic data quantify the flow field properties (rather than the optical quantification of the integrated effect of the flow field) aerodynamic scaling relationships used throughout the aircraft industry can be used to extrapolate the wind tunnel data to flight conditions. These relationships are not always known exactly; but, for large scale turrets in flight, propagation of coherent radiation for aft-looking angles at short wavelengths without some sort of flow control would appear to be impractical based on any reasonable extrapolation of the wind tunnel data to flight conditions.

V. RECOMMENDATIONS FOR FURTHER WORK

Results from the present large-scale wind tunnel test indicate that potentially serious optical wavefront distortion can occur when looking aft from an on-gimbal type airborne turret. As in all present day aerodynamic testing, wind tunnel results are a useful guide to flight situations; however, for the complicated, three-dimensional flows, scaling the wind tunnel data to flight conditions is not straightforward. Flight testing actual hardware is costly; although, considering the serious nature of the findings of this study, the known technology of both aerodynamic and optical instrumentation should be used to evaluate a full-scale airborne system.

Turret positions investigated in this study were limited to zero elevation angle for various azimuth angles. Since flight scenarios envision elevation angles up to 90 deg, the effect of the full three-dimensional flow field over the top of the turret on optical performance should be investigated. This investigation could be carried out in either large- or small-scale wind tunnel tests using the same instrumentation as used here.

Further wind tunnel testing to establish or verify known aerodynamic scaling relationships should be conducted with extensive unsteady instrumentation that allows the entire turbulence stress tensor to be determined throughout the turret flow field. Only with this type of turbulence data can today's powerful numerical calculation procedures be used to predict the complex turret flow field to an engineering accuracy.

Little is known about the spatial and temporal statistics of the optical wavefront distortion. Large spatial variances (of order two or three) have been observed particularly at the 90-deg turret position. The effect of spatially nonuniform optical distortion of this magnitude may be very important. The importance may be heightened for cases in which the propagated beam is already spatially nonuniform. Further investigations should be conducted into the spatial variation of wavefront distortion, including the possibility of optically tailoring the propagated beam to minimize its losses.

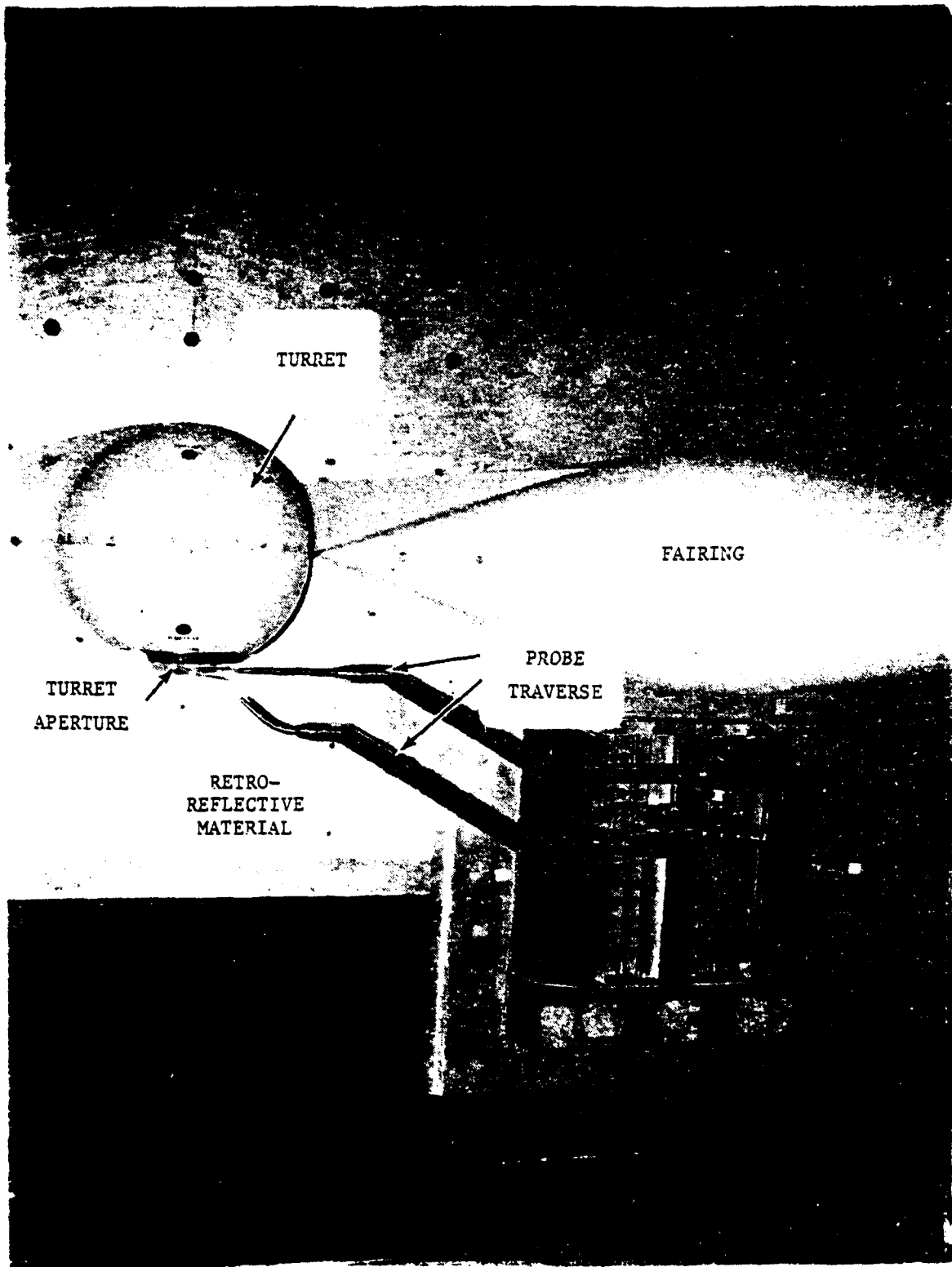


FIGURE 1. PHOTOGRAPH OF TURRET AND FAIRING MODEL MOUNTED IN THE NASA-AMES 14-FT WIND TUNNEL

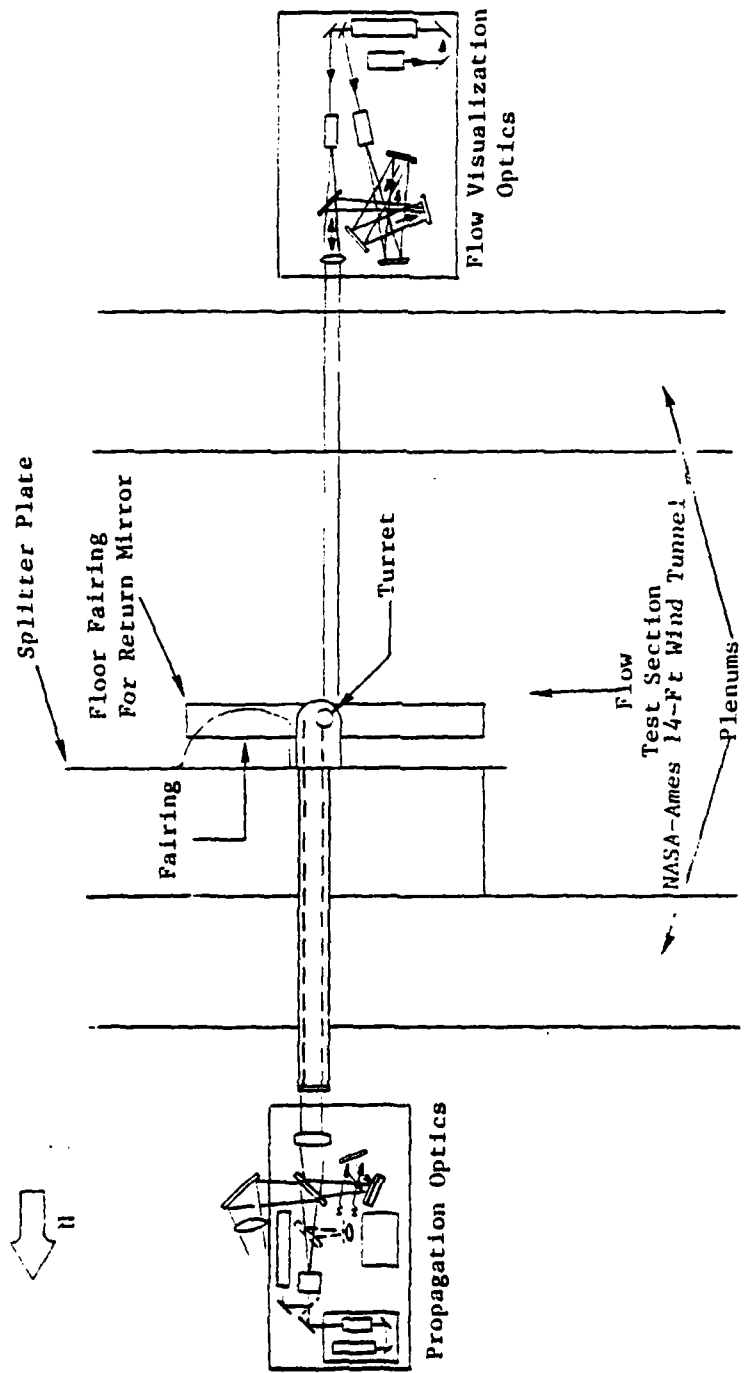


FIGURE 2. SCHEMATIC OF OPTICAL DIAGNOSTIC SYSTEMS USED IN THE PRESENT STUDY

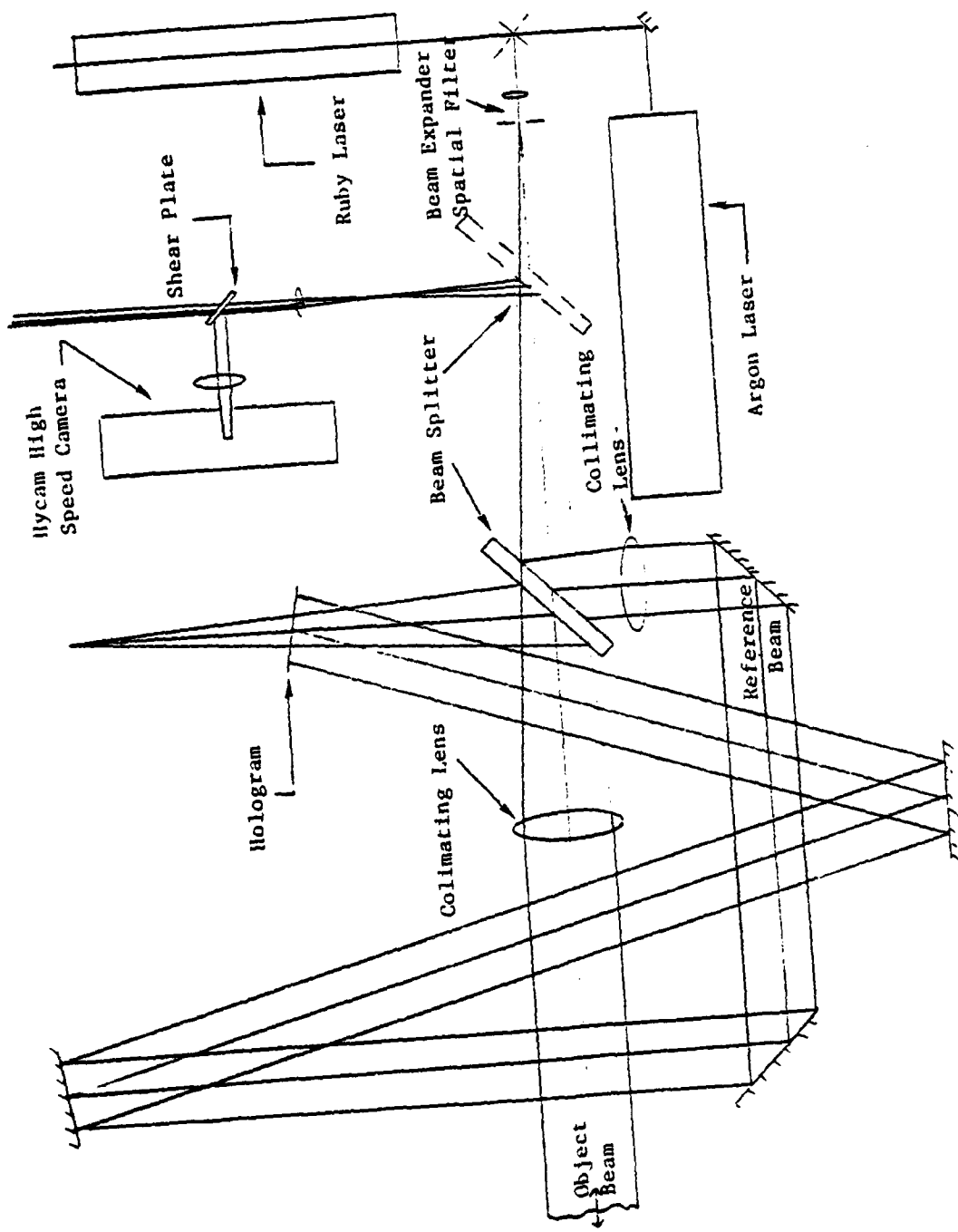


FIGURE 3. SCHEMATIC OF PROPAGATION HOLOGRAPHY SYSTEM

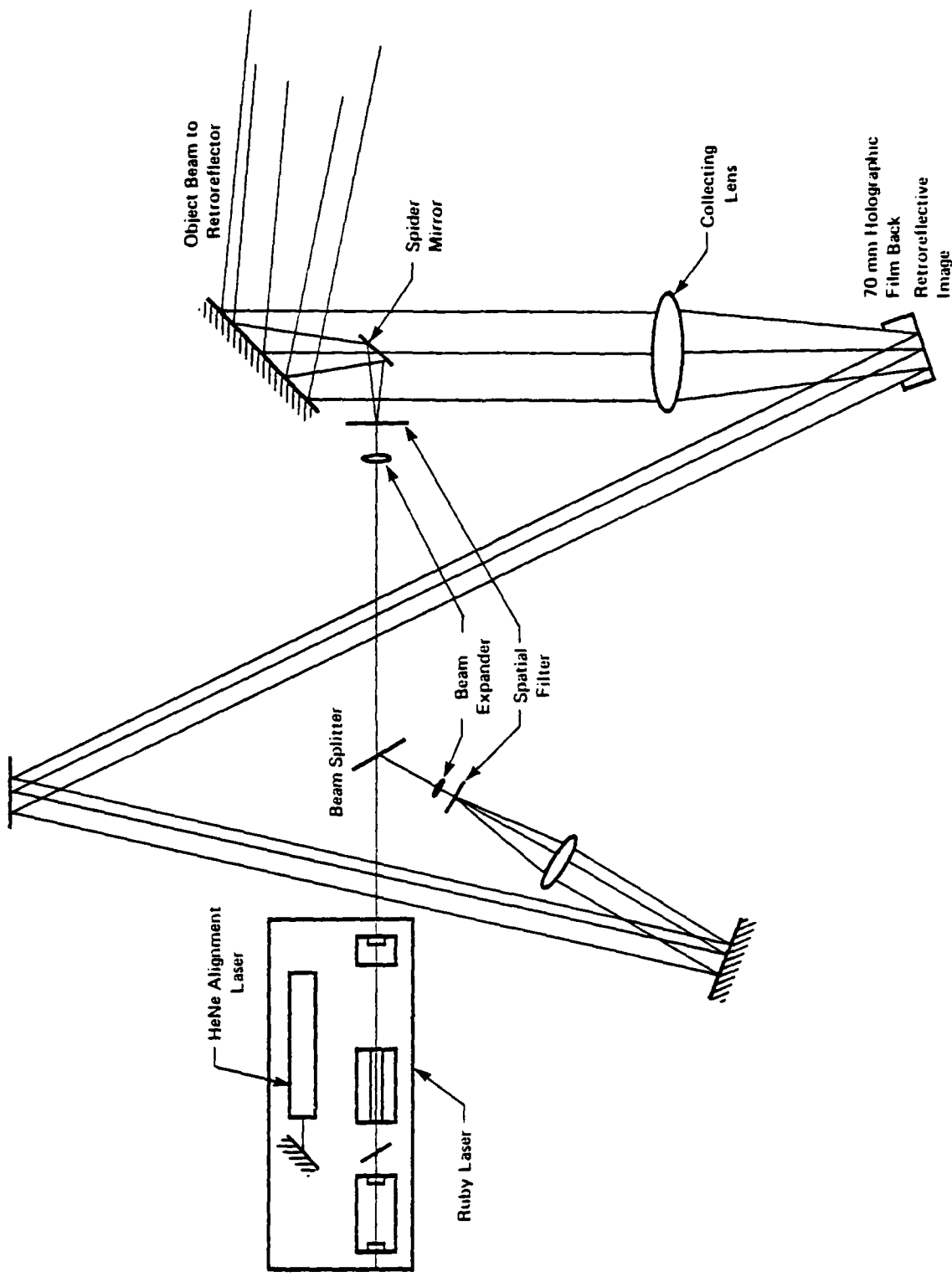


FIGURE 4. SCHEMATIC OF FLOW VISUALIZATION HOLOGRAPHY SYSTEM



FIGURE 5. COMPOSITE OF MODEL PHOTOGRAPH AND FLOW VISUALIZATION
INTERFROGRAM, $M = 0.55$

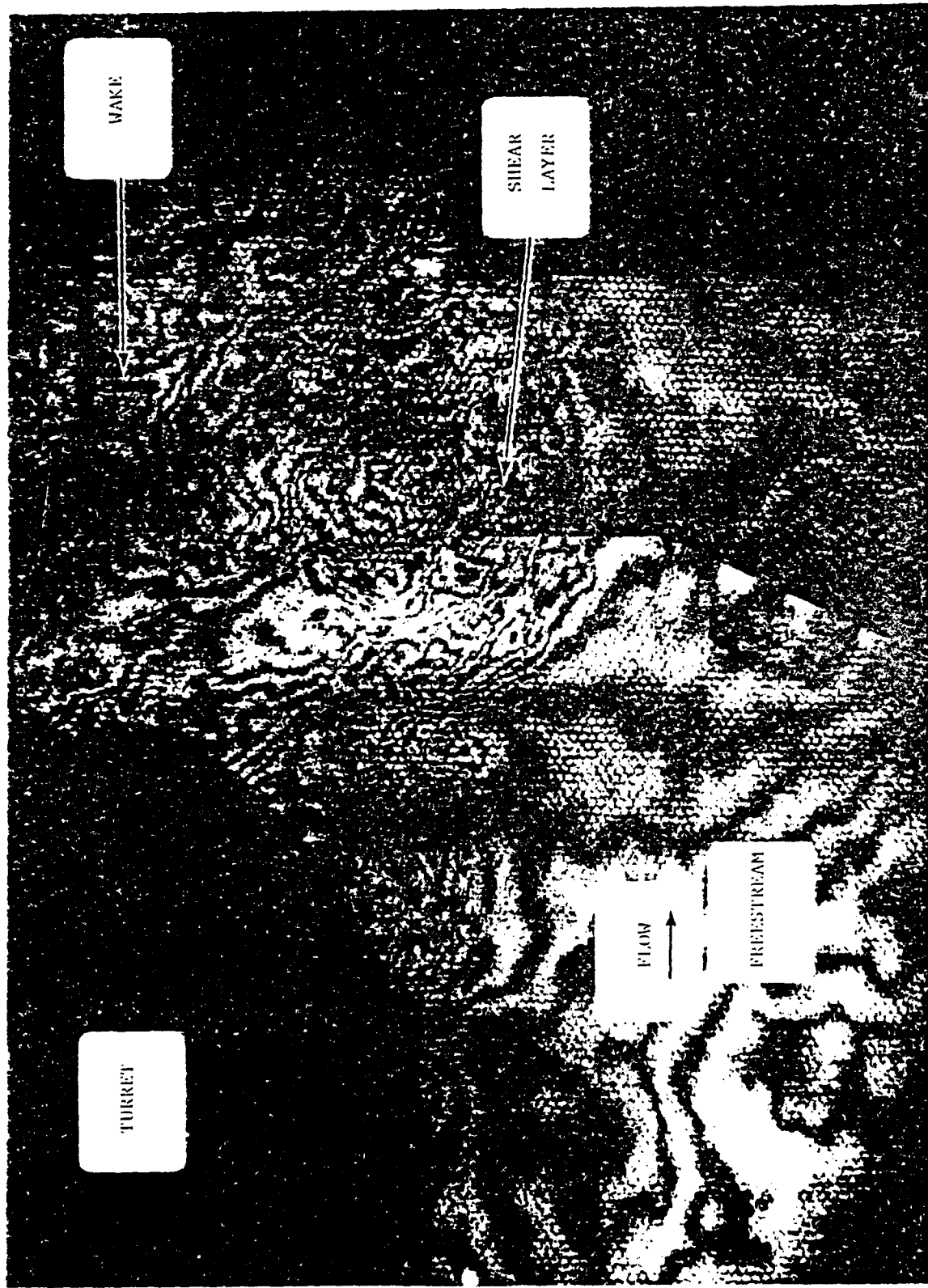


FIGURE 6. LOW MACH NUMBER FLOW VISUALIZATION
INTERFEROGRAM, $M = 0.55$

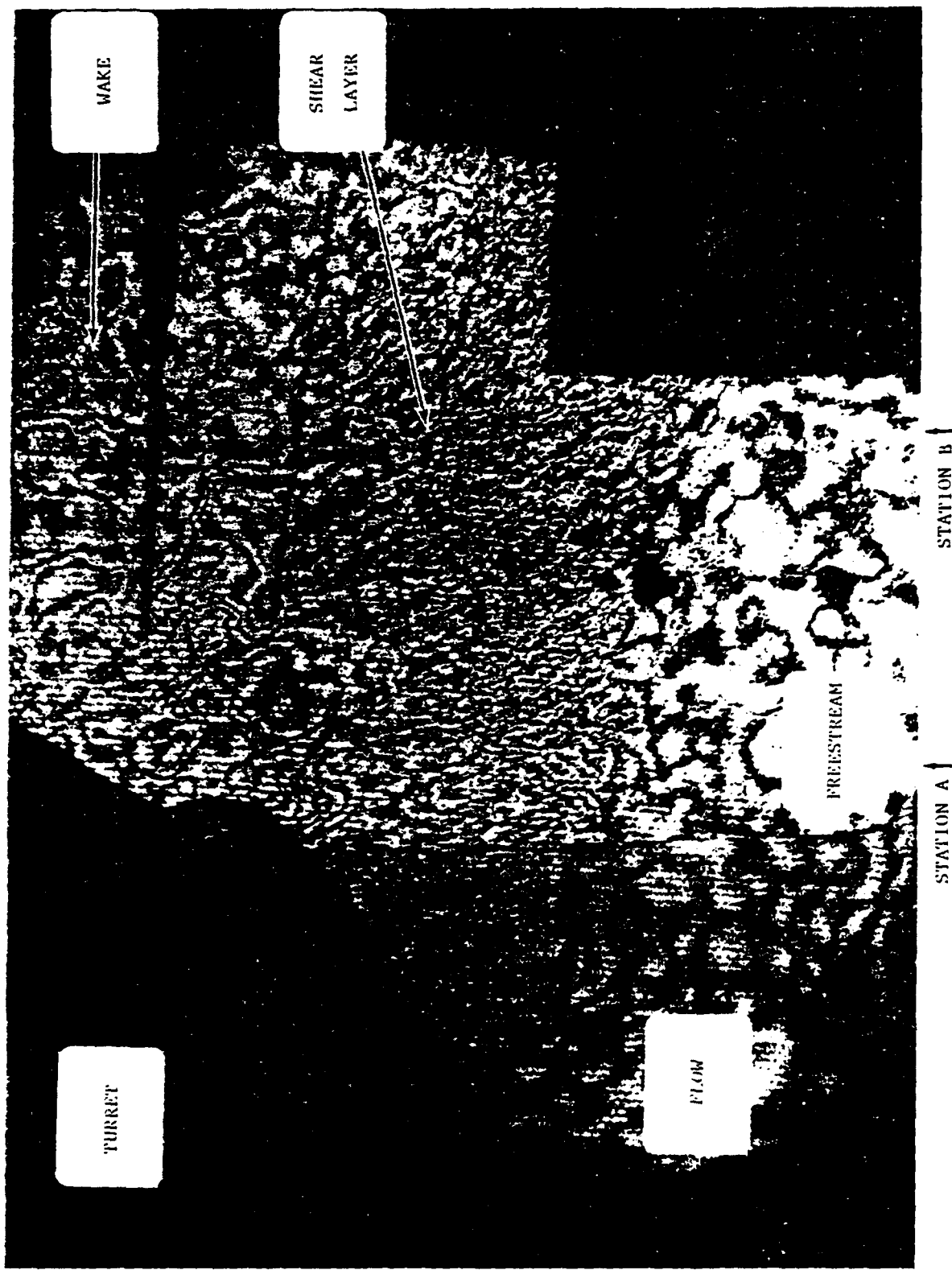
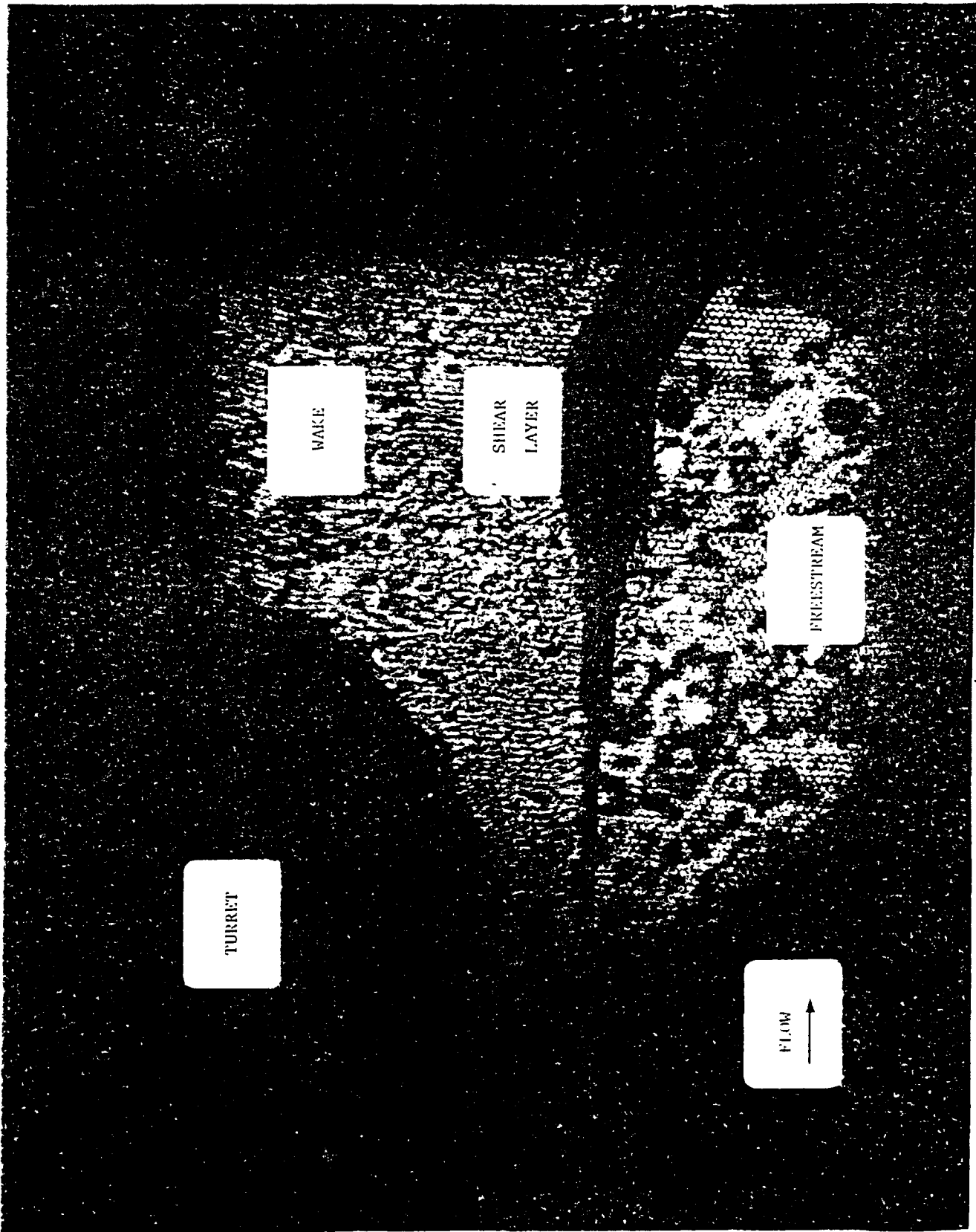


FIGURE 7. INTERMEDIATE MACH NUMBER FLOW VISUALIZATION
INTERFEROGRAM, $M = 0.65$

FIGURE 8. HIGH MACH-NUMBER FLOW VISUALIZATION
PROVIDED BY DODGE & CO.



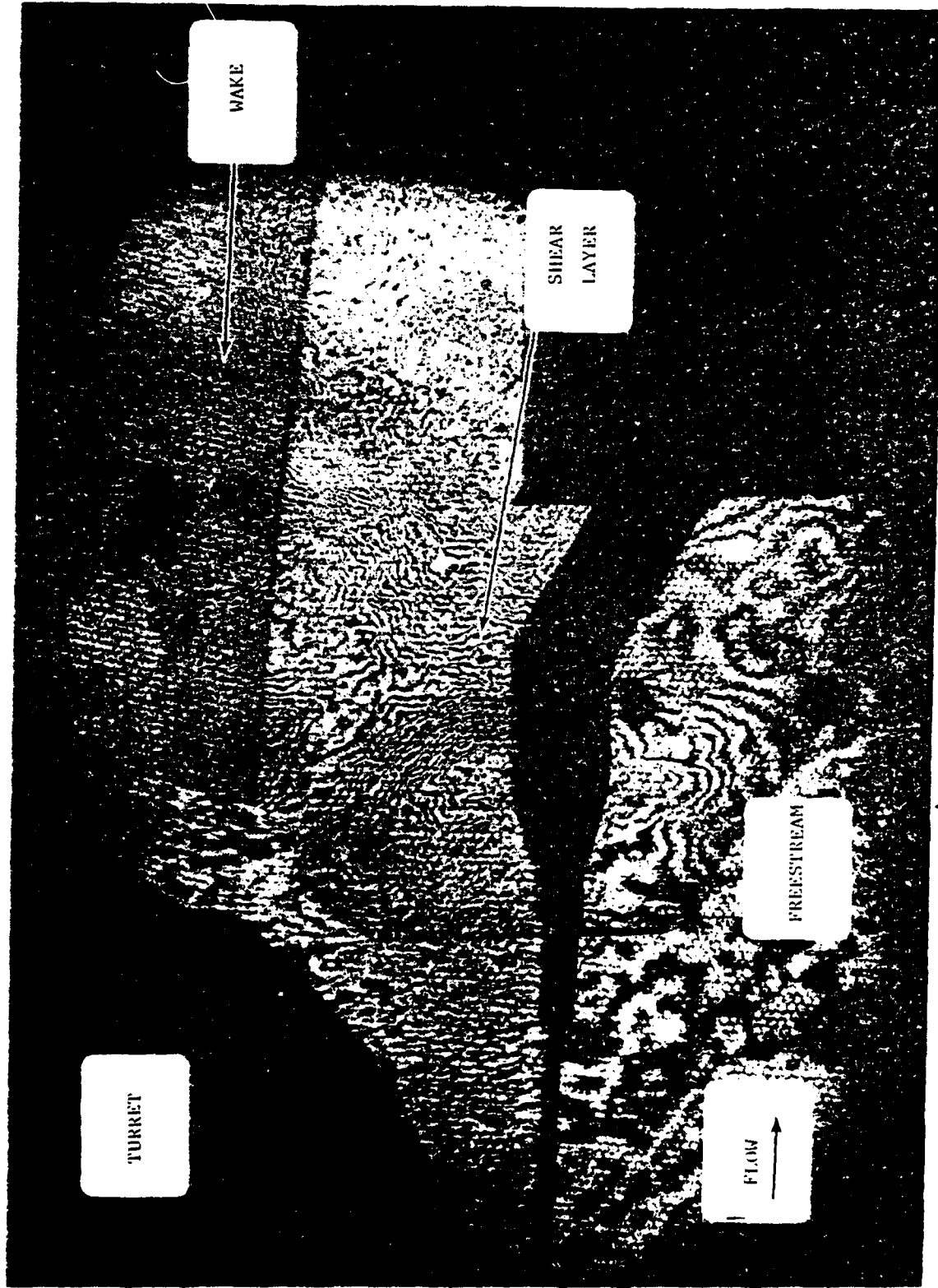


FIGURE 9. HIGH MACH NUMBER FLOW VISUALIZATION INTERFEROGRAM, $M = 0.75$, WITH LARGE SCALE EVENT.

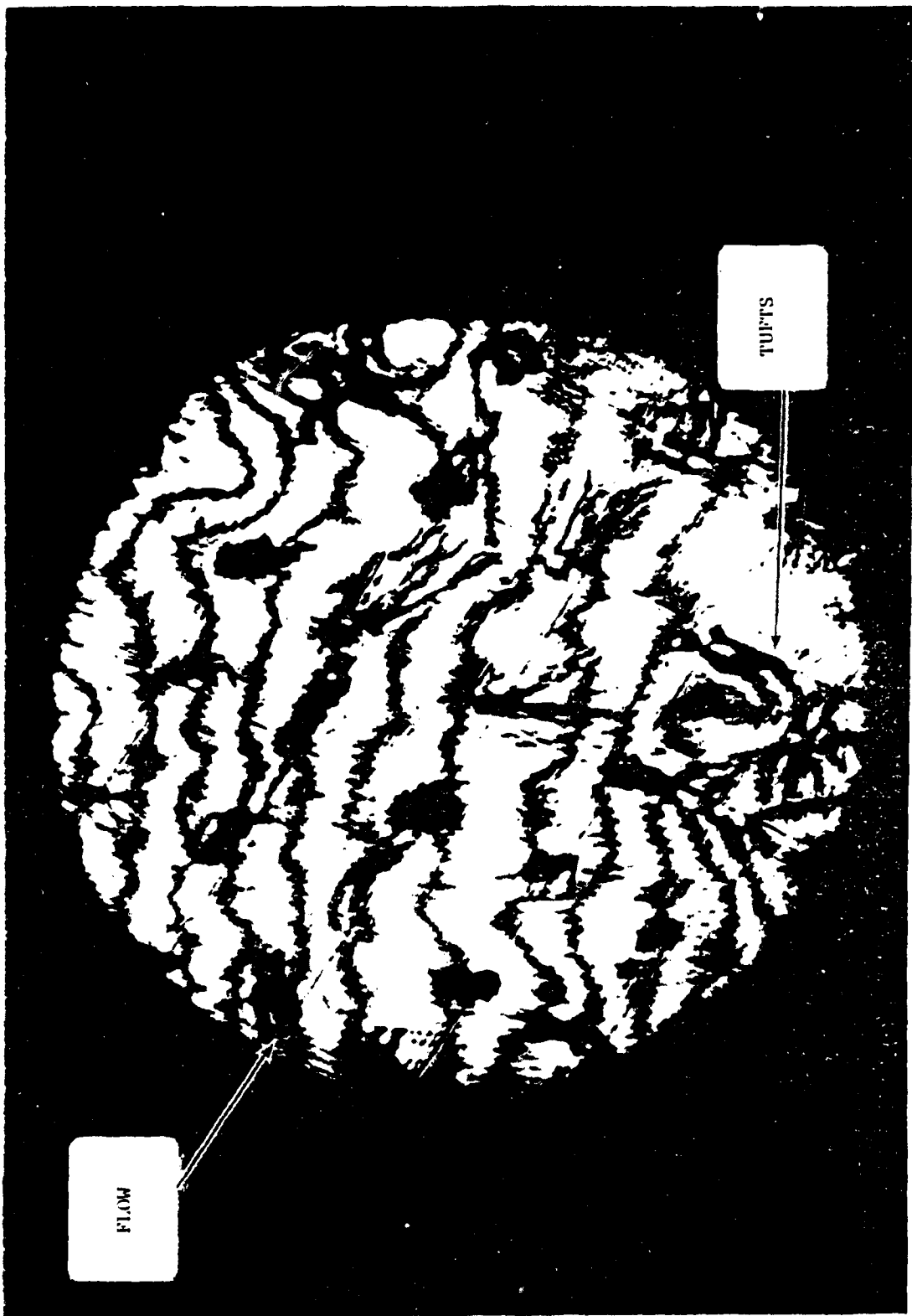
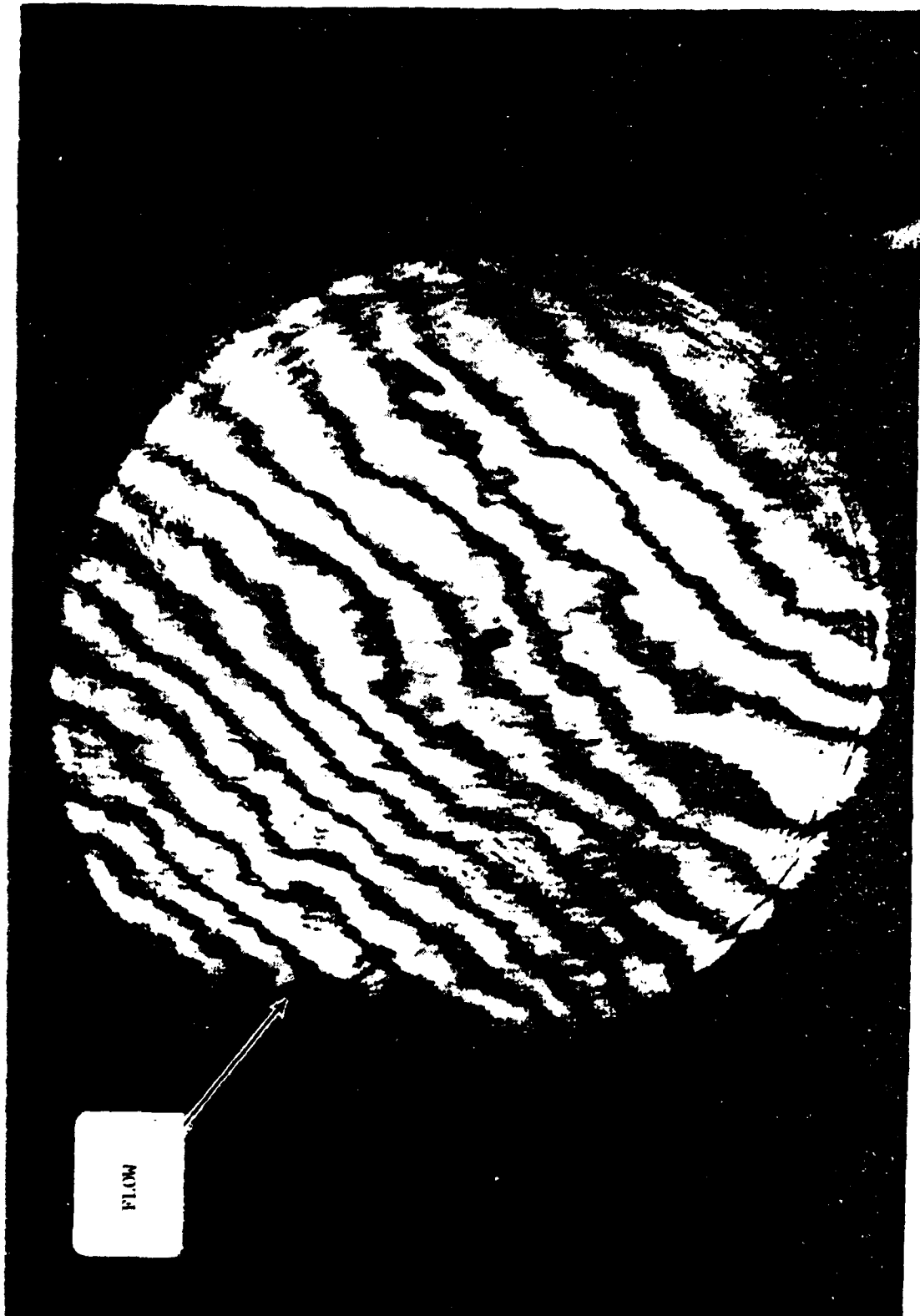
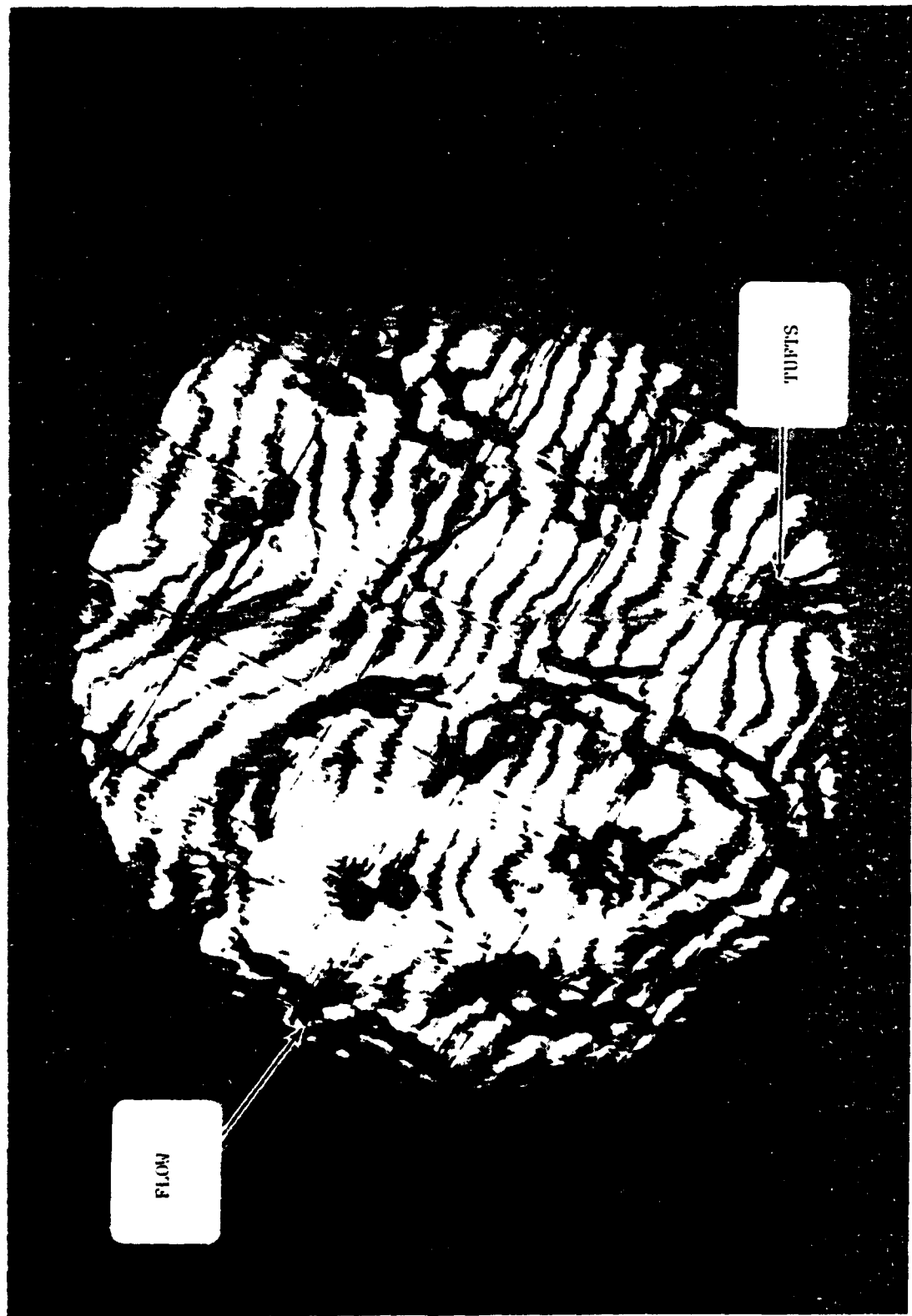


FIGURE 10. LOW MACH NUMBER PROPAGATION INTERFEROGRAM,
 $M = 0.55$, $\theta = 60$ deg
(a) OPEN PORT

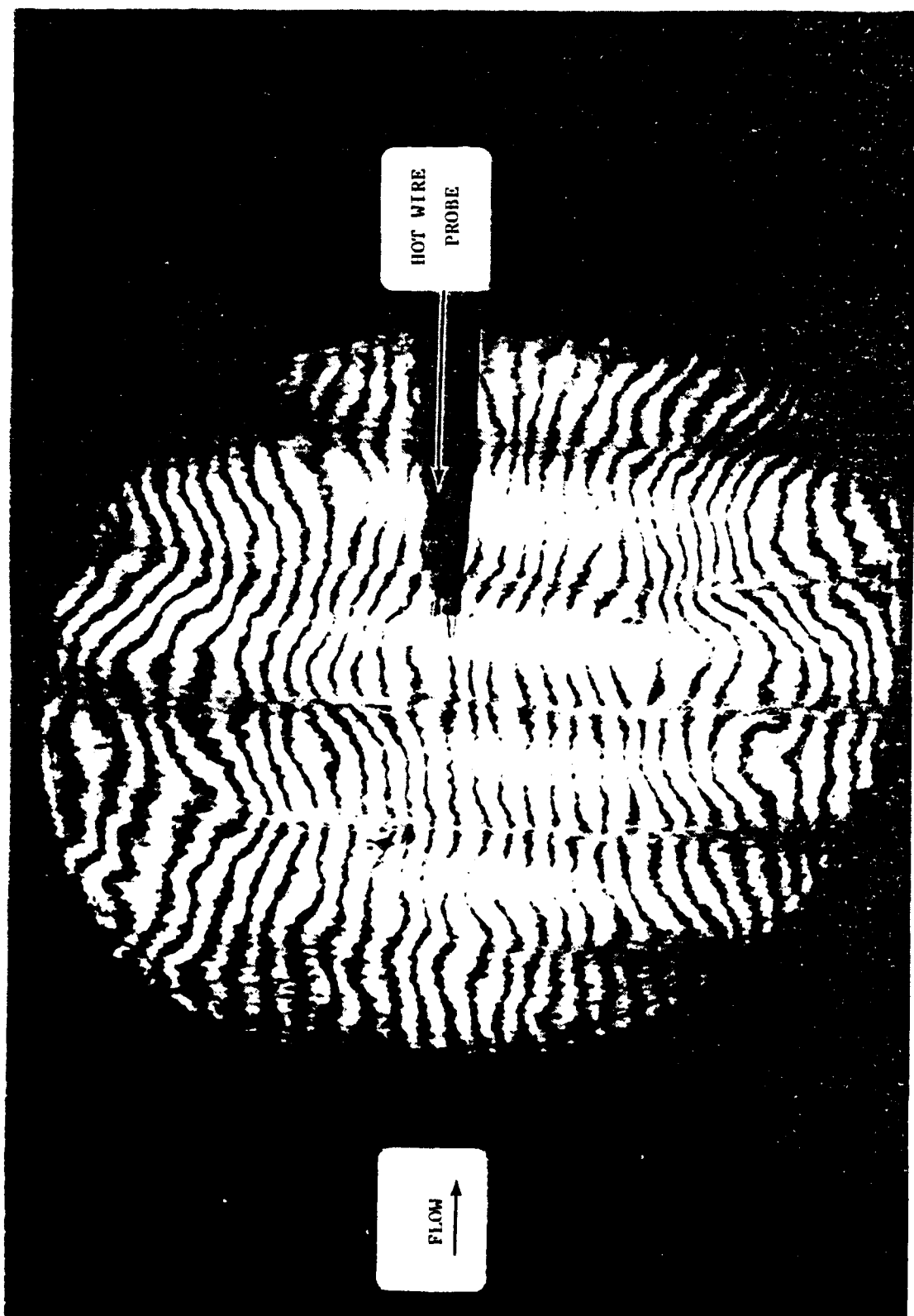
(b) WINDOWED PORT
FIGURE 10. (CONCLUDED)





(a) $\theta = 60$ deg

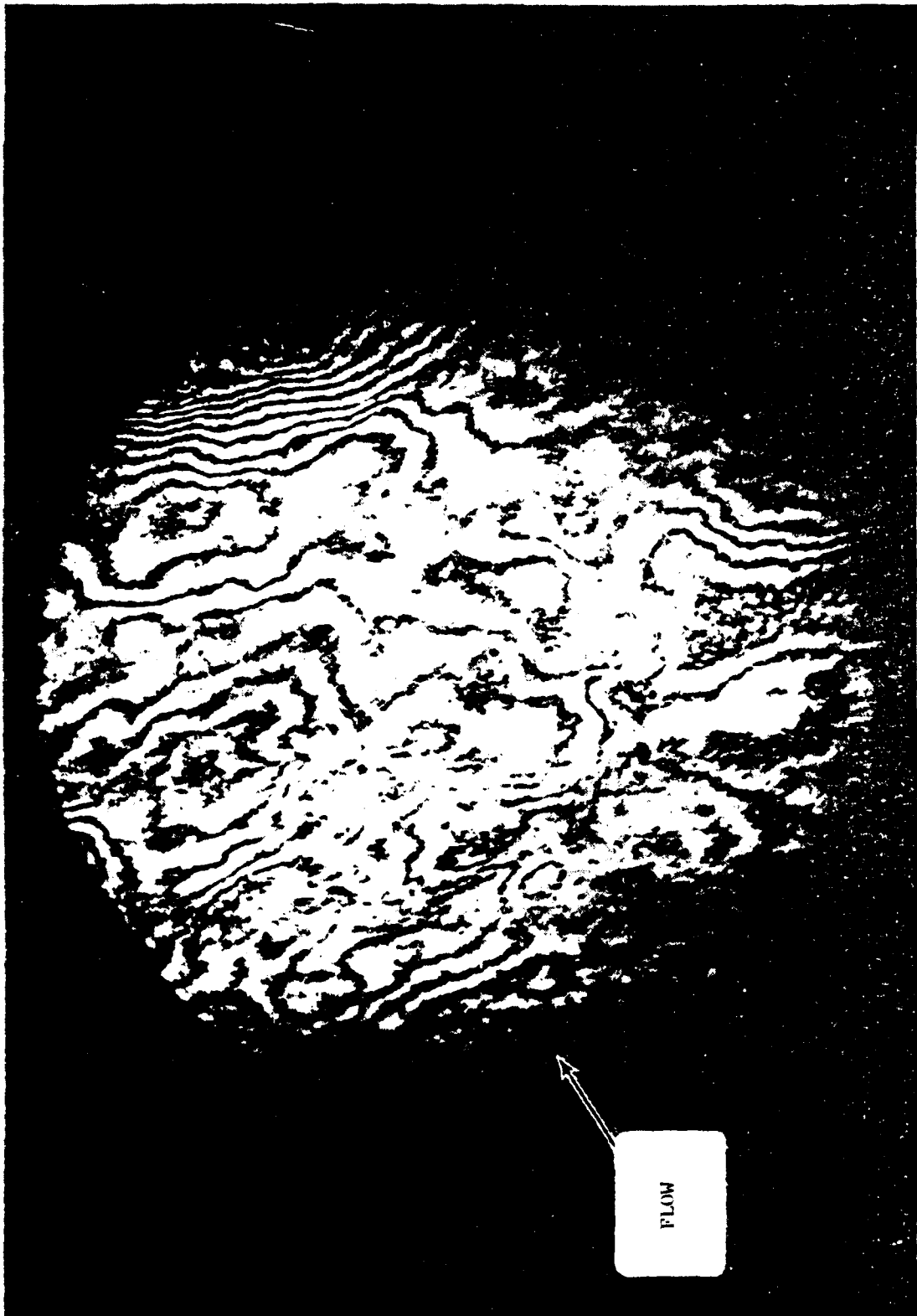
FIGURE 11. INTERMEDIATE MACH NUMBER PROPAGATION INTERFEROGRAM, $M = 0.65$, OPEN PORT



(b) $\theta = 90$ deg

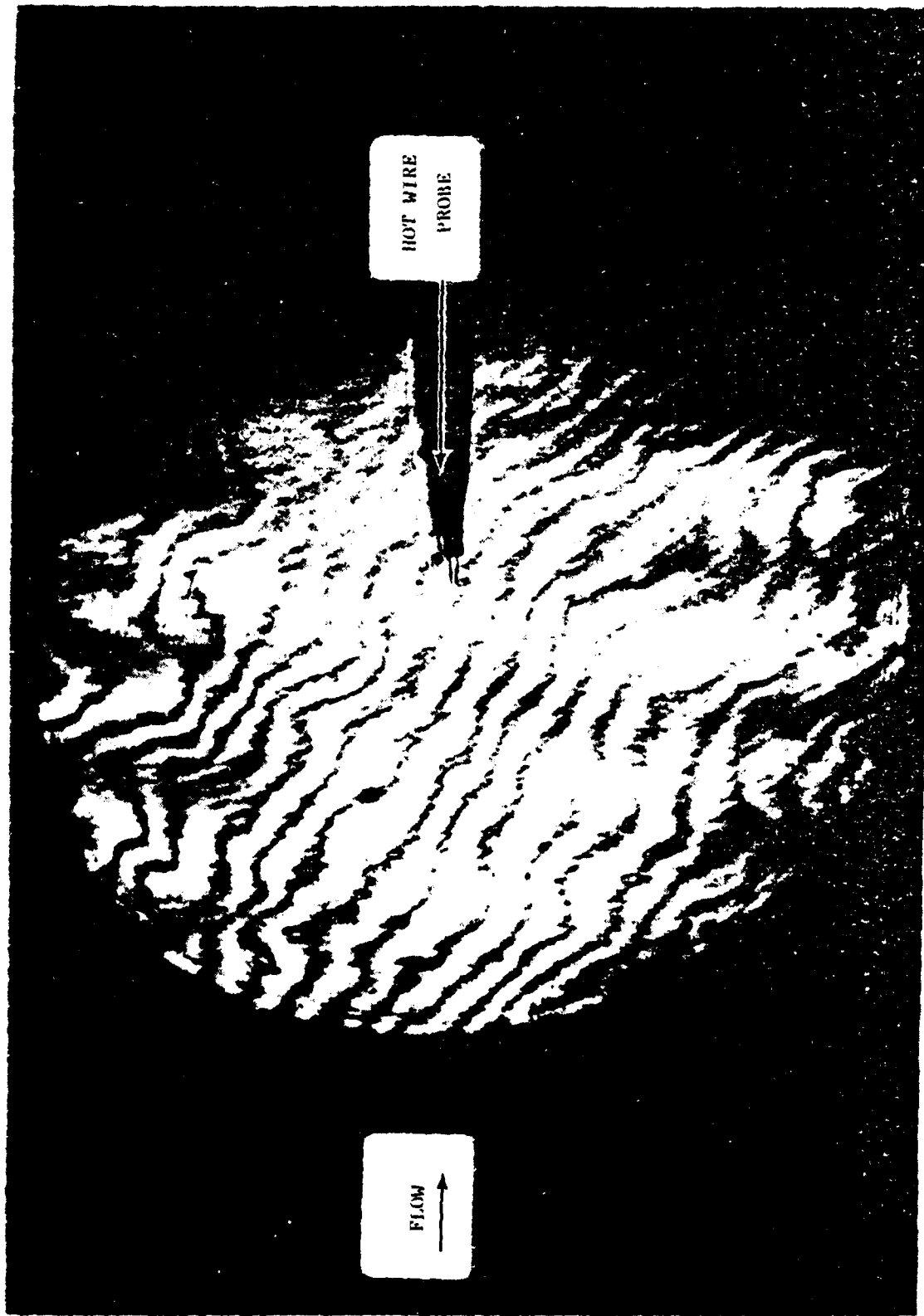
FIGURE 11. (CONTINUED)

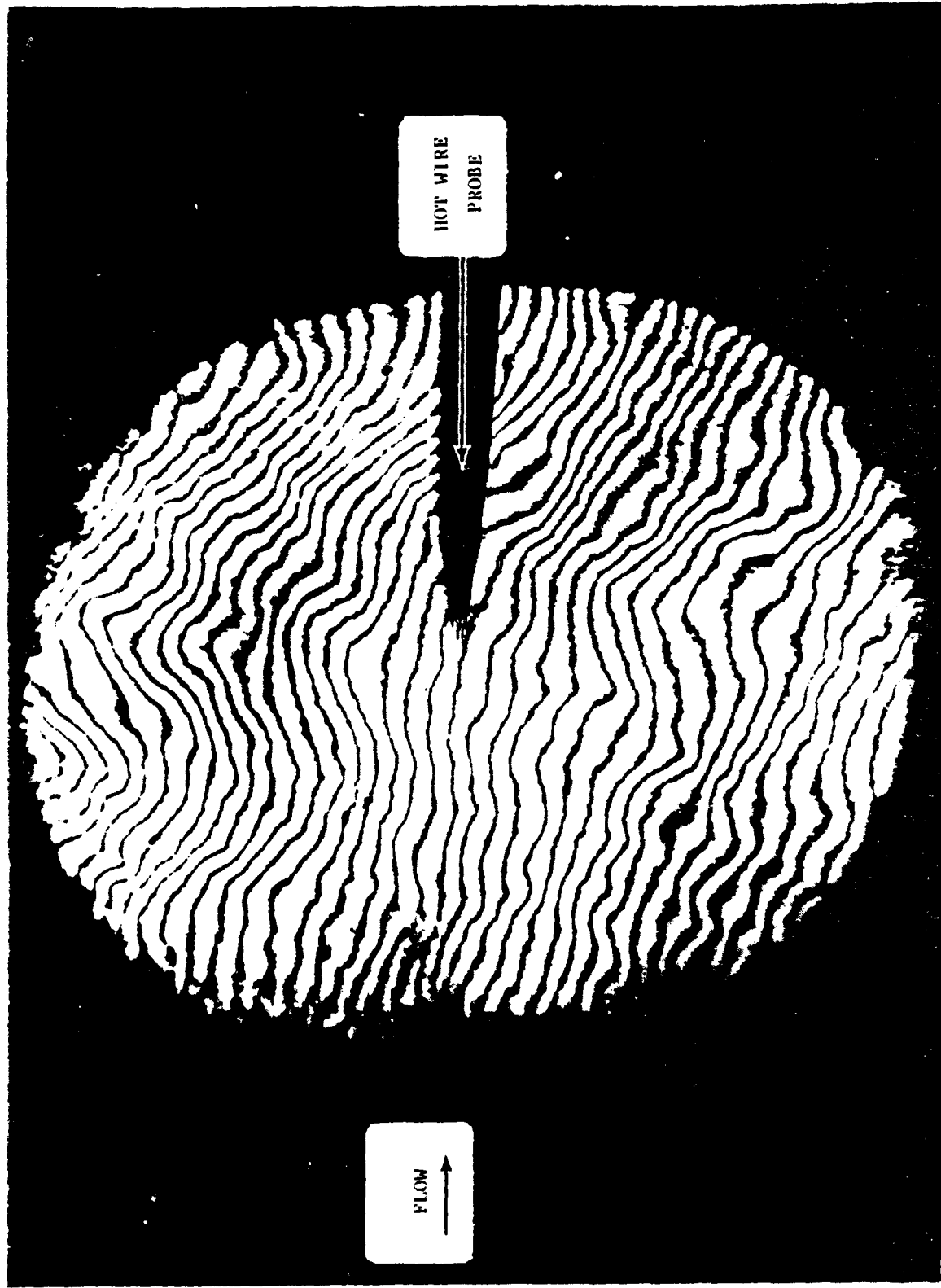
(c) $\theta = 120$ deg
FIGURE 11. (CONCLUDED)



(a) $M = 0.55$

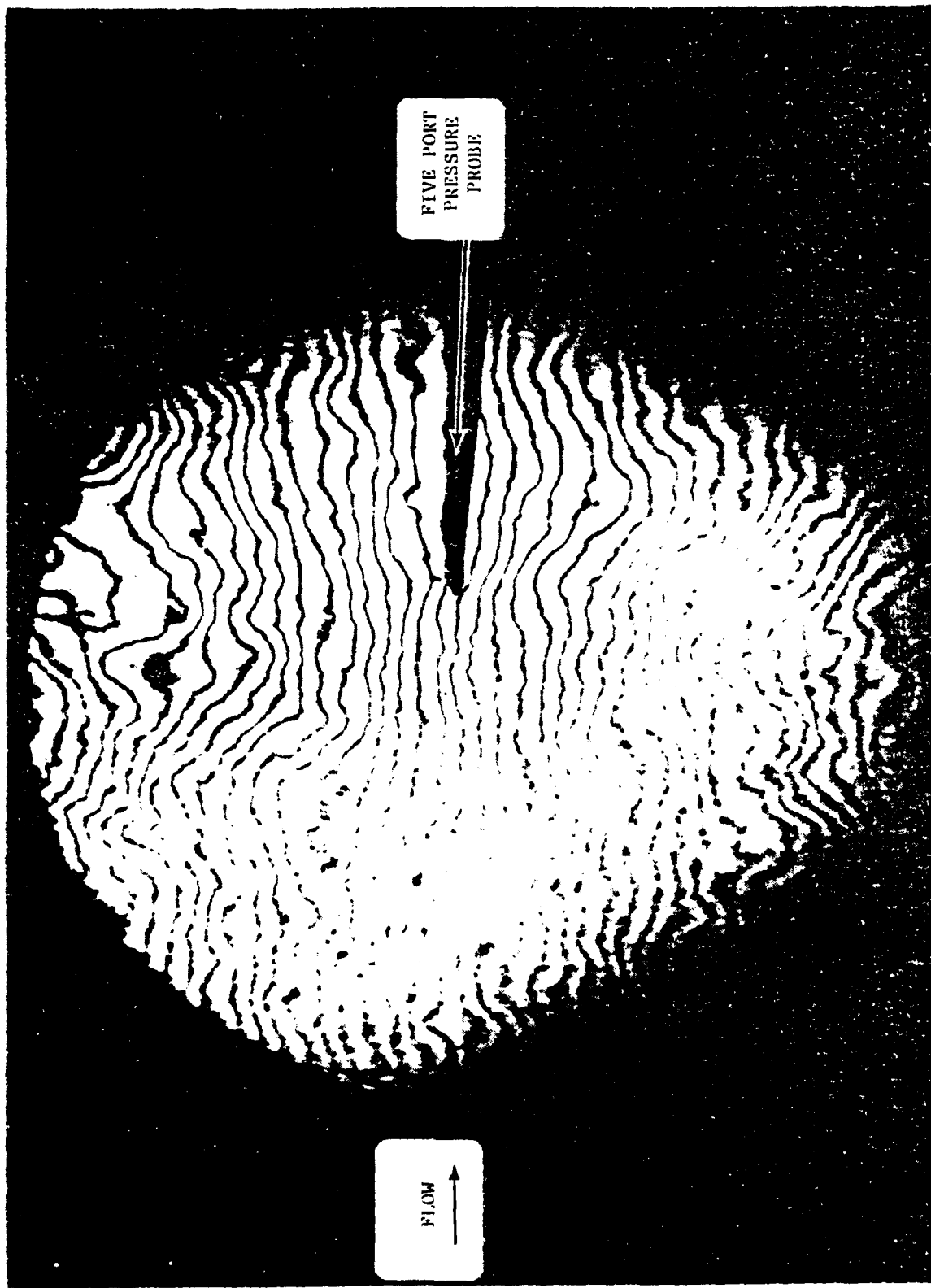
FIGURE 12. PROPAGATION INTERFEROGRAM, $\theta = 90$ deg, OPEN PORT



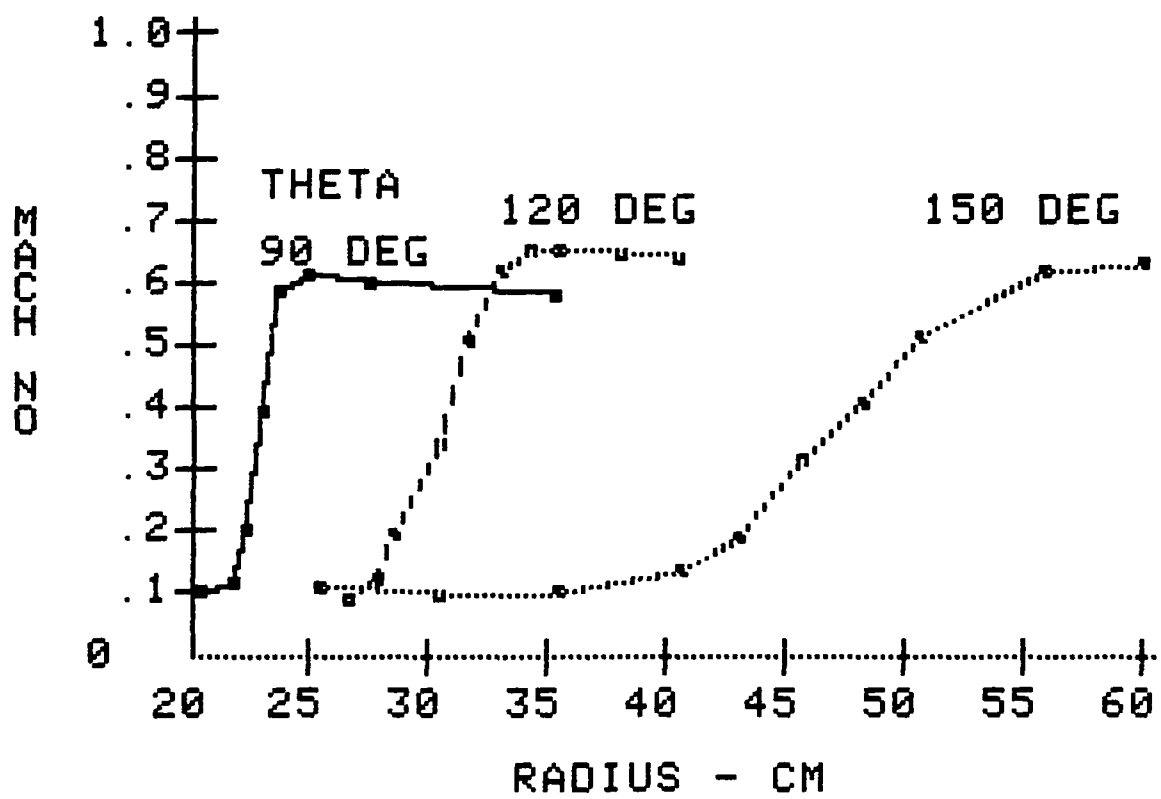


(b) $M = 0.65$

FIGURE 12. (CONTINUED)

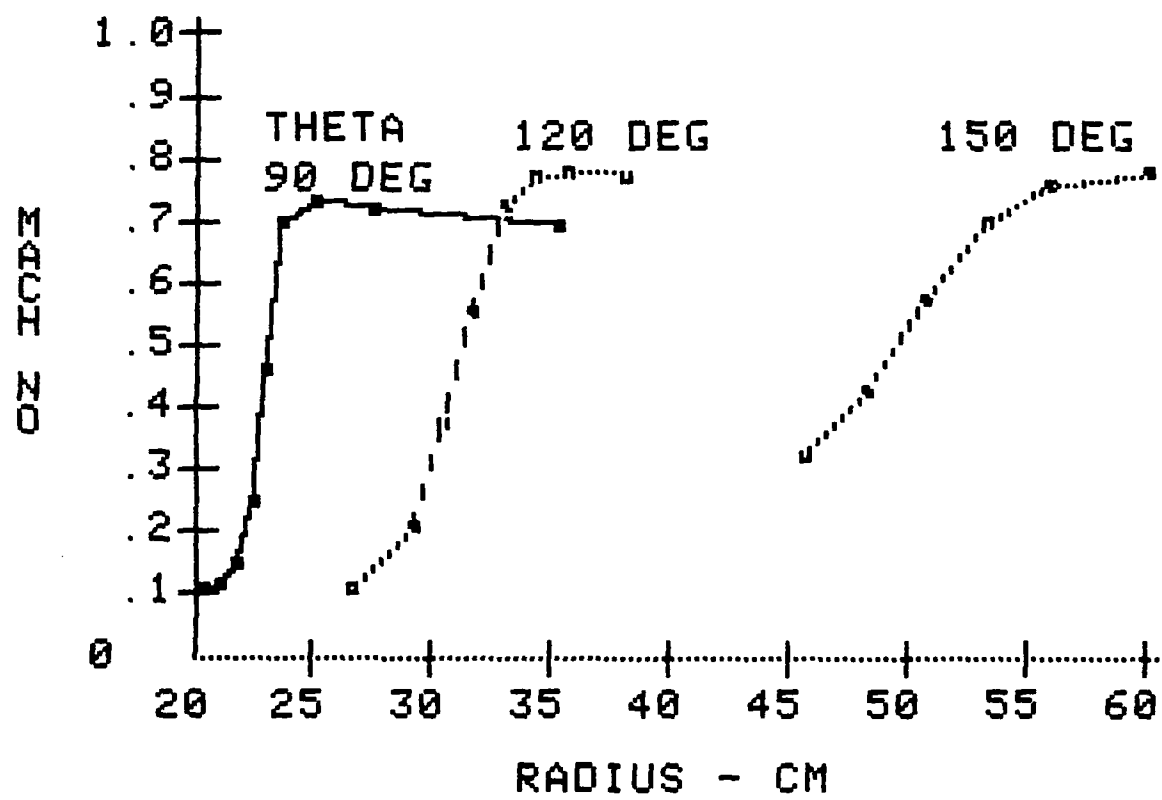


(c) $M = 0.75$
FIGURE 12. (CONCLUDED)



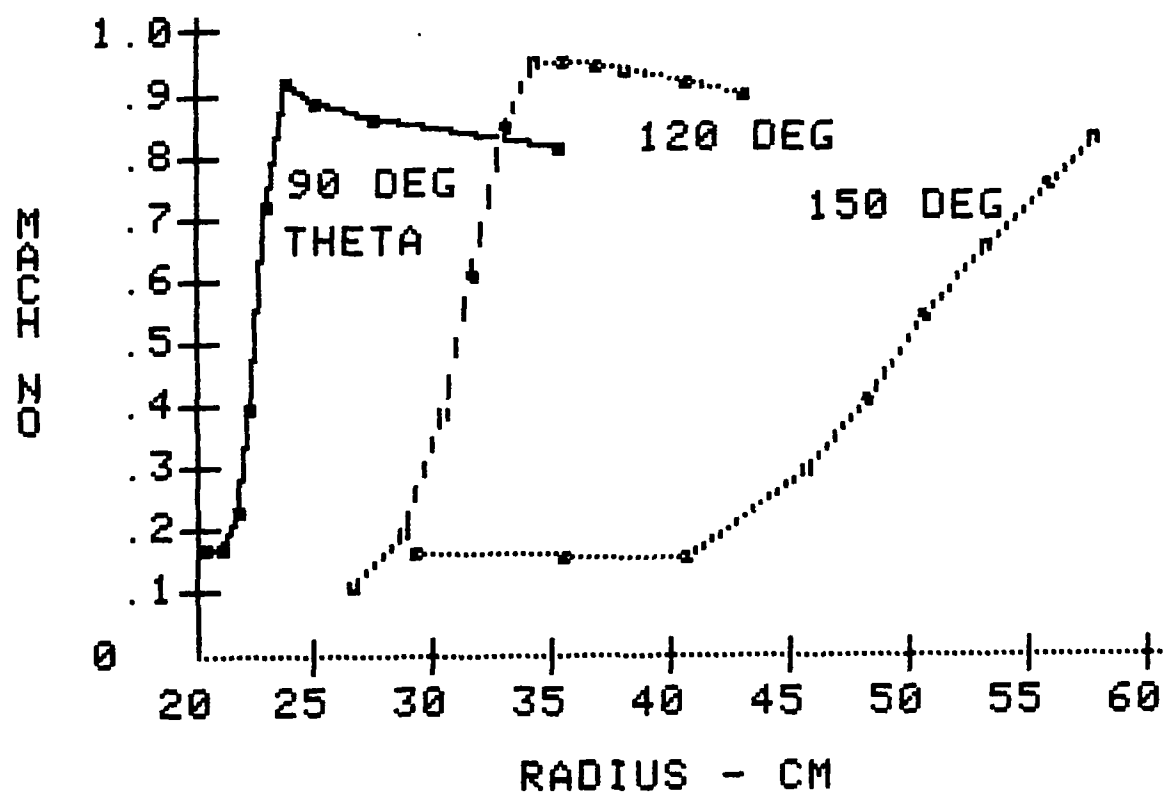
(a) $M = 0.55$

FIGURE 13. DISTRIBUTION OF MEAN MACH NUMBER, M.



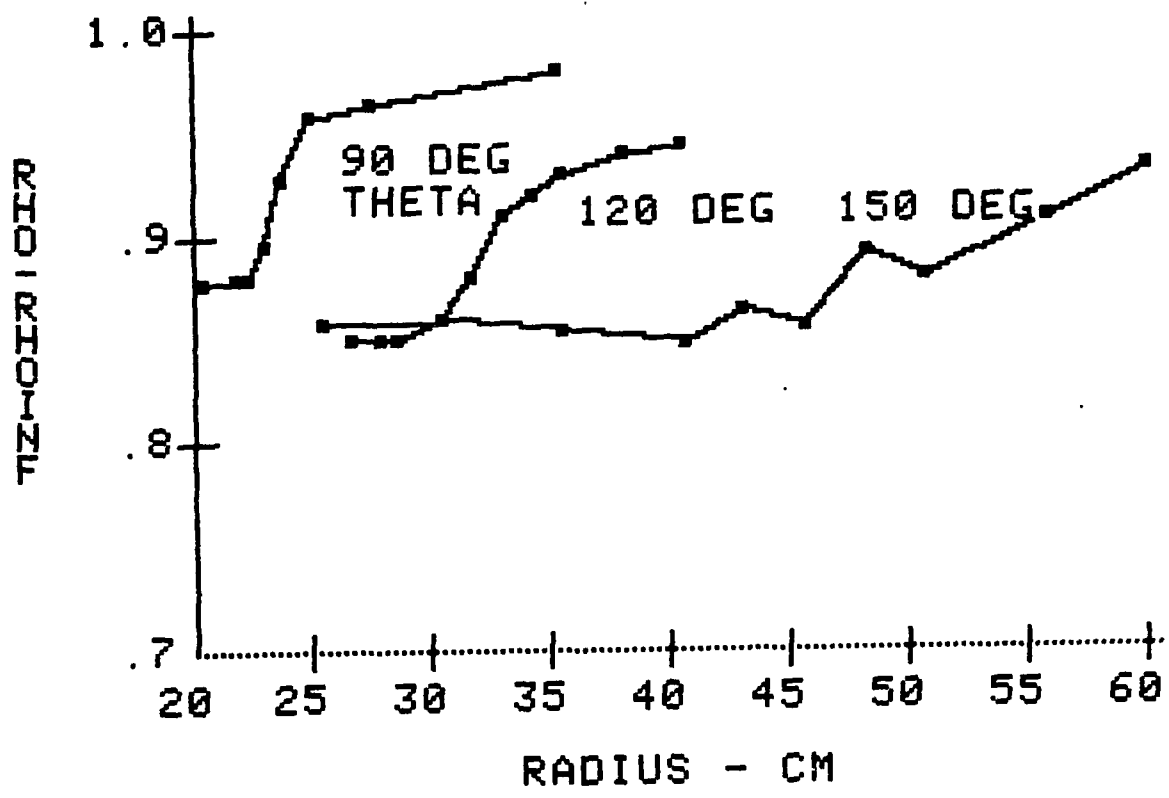
(b) $M = 0.65$

FIGURE 13. (CONTINUED)



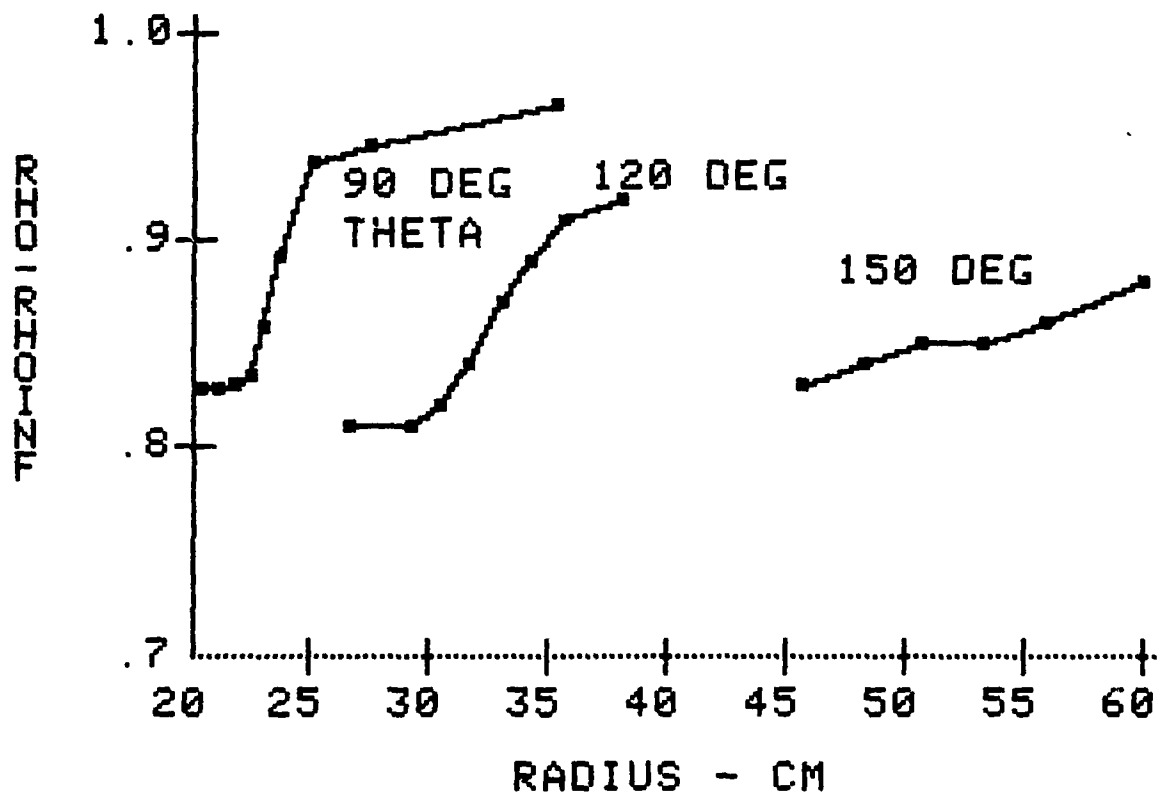
(c) $M = 0.75$

FIGURE 13. (CONCLUDED)

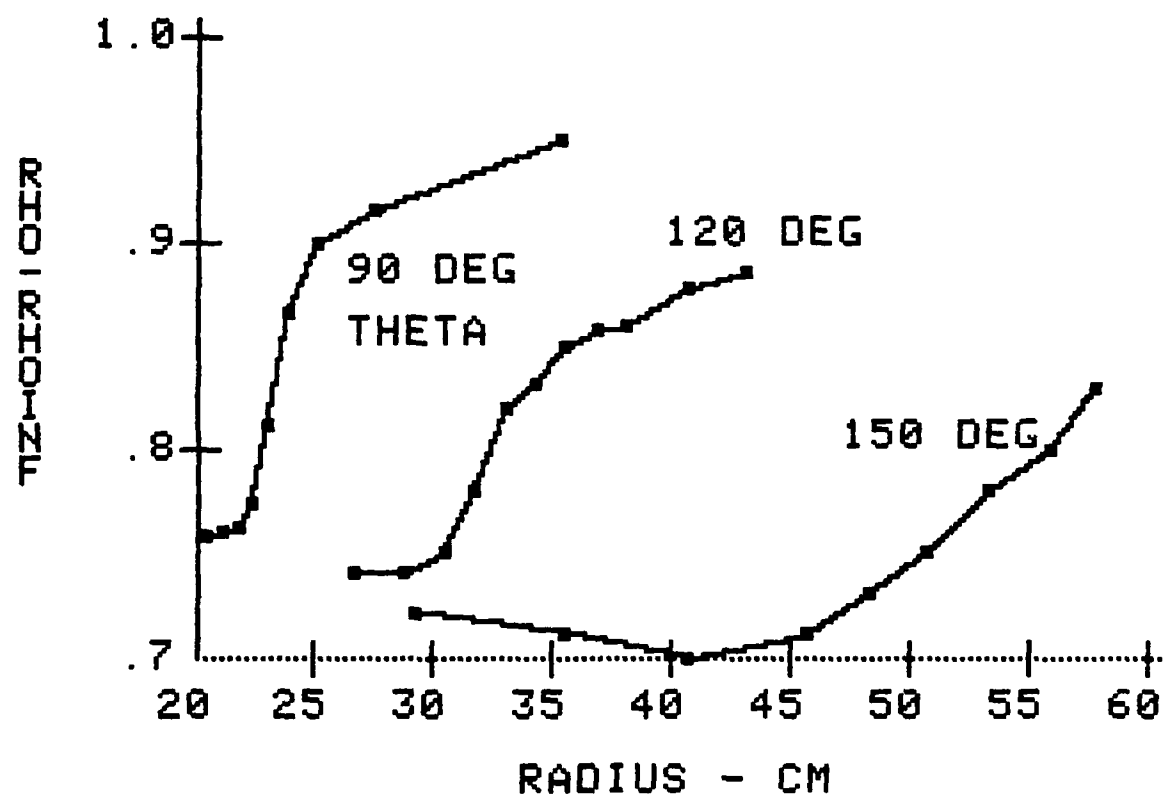


(a) $M = 0.55$

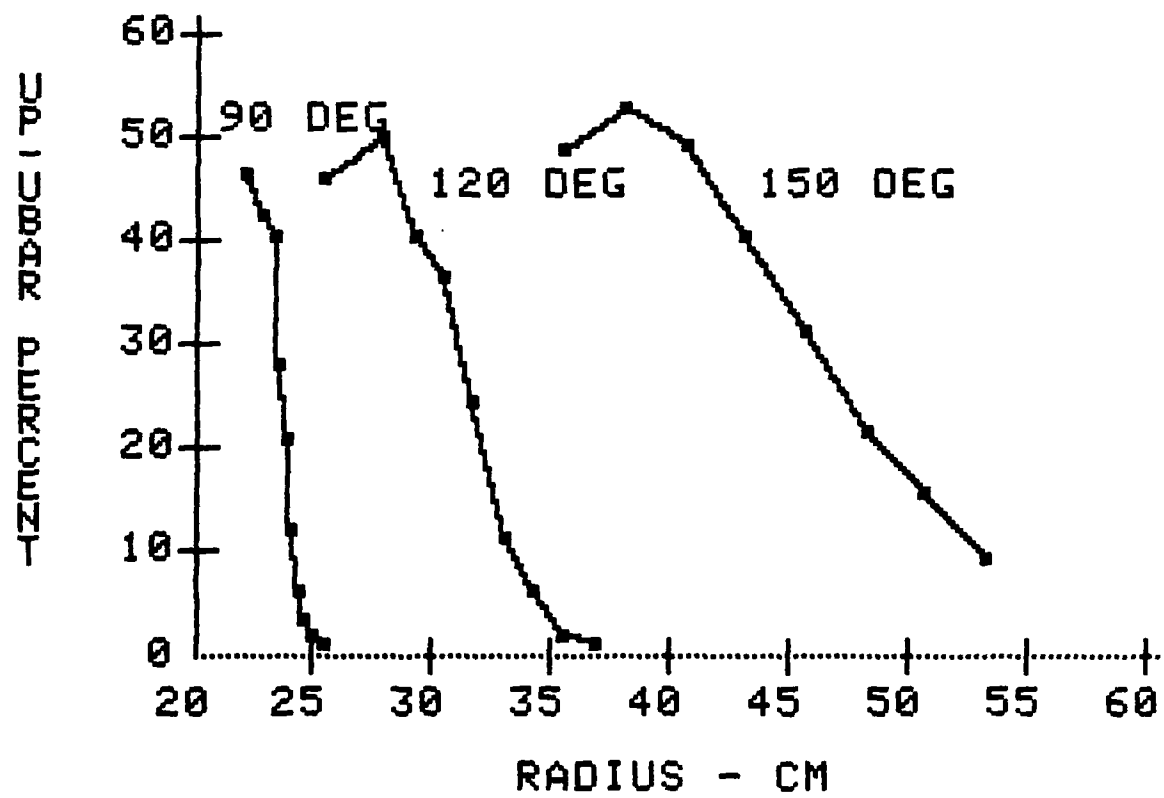
FIGURE 14. DISTRIBUTION OF MEAN DENSITY, $\bar{\rho}/\rho_\infty$.



(b) $M = 0.65$
FIGURE 14. (CONTINUED)

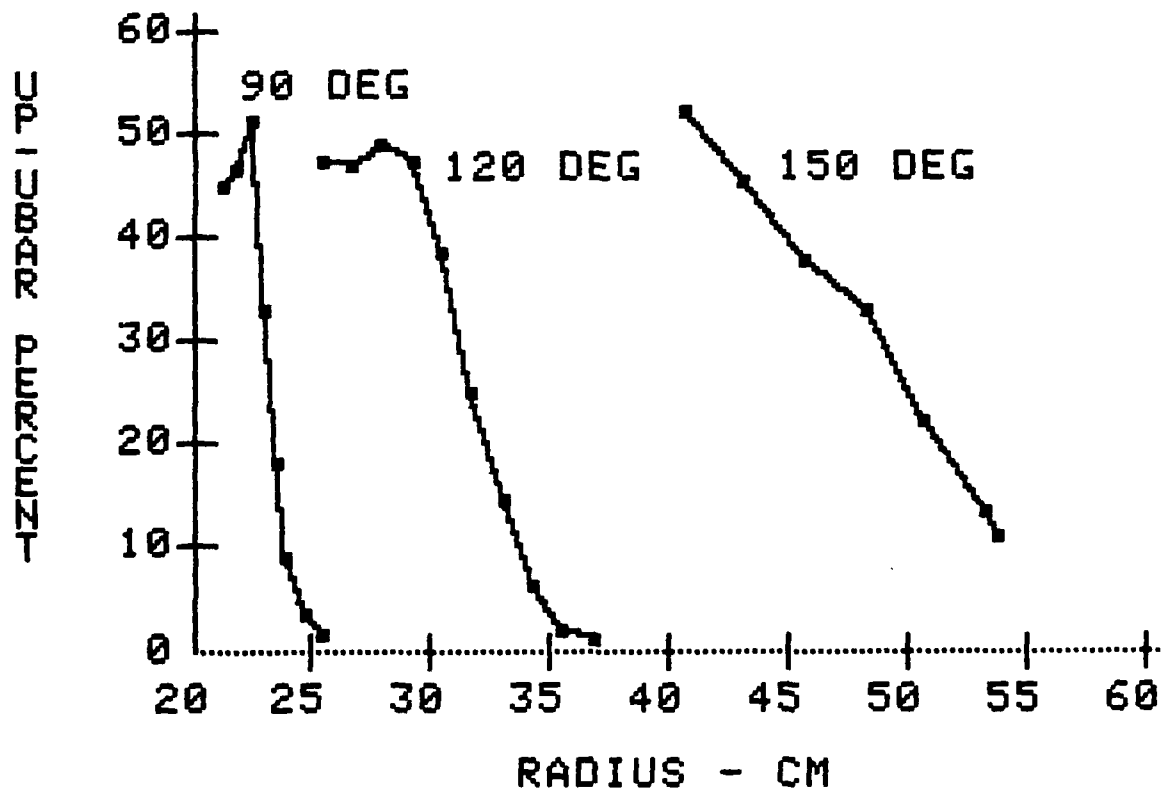


(c) $M = 0.75$
FIGURE 14. (CONCLUDED)



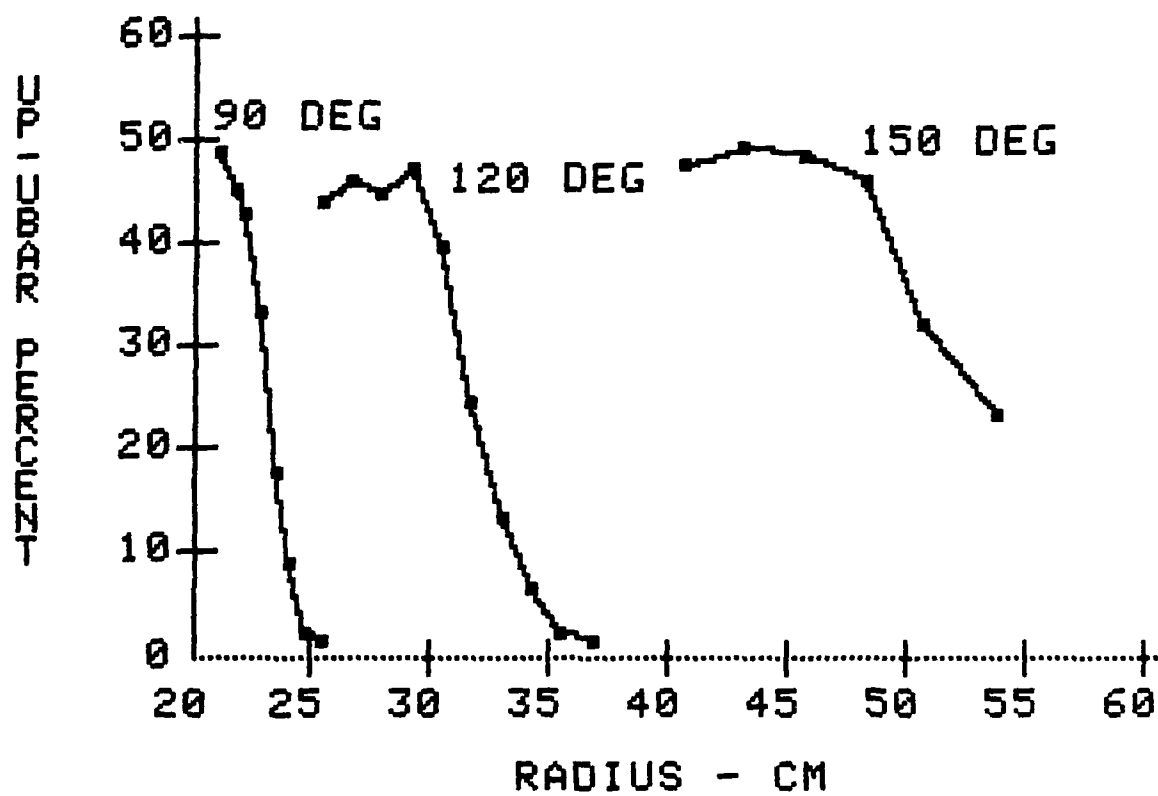
(a) $M = 0.55$

FIGURE 15. DISTRIBUTION OF FLUCTUATING VELOCITY, $\langle u' \rangle / \bar{u}$

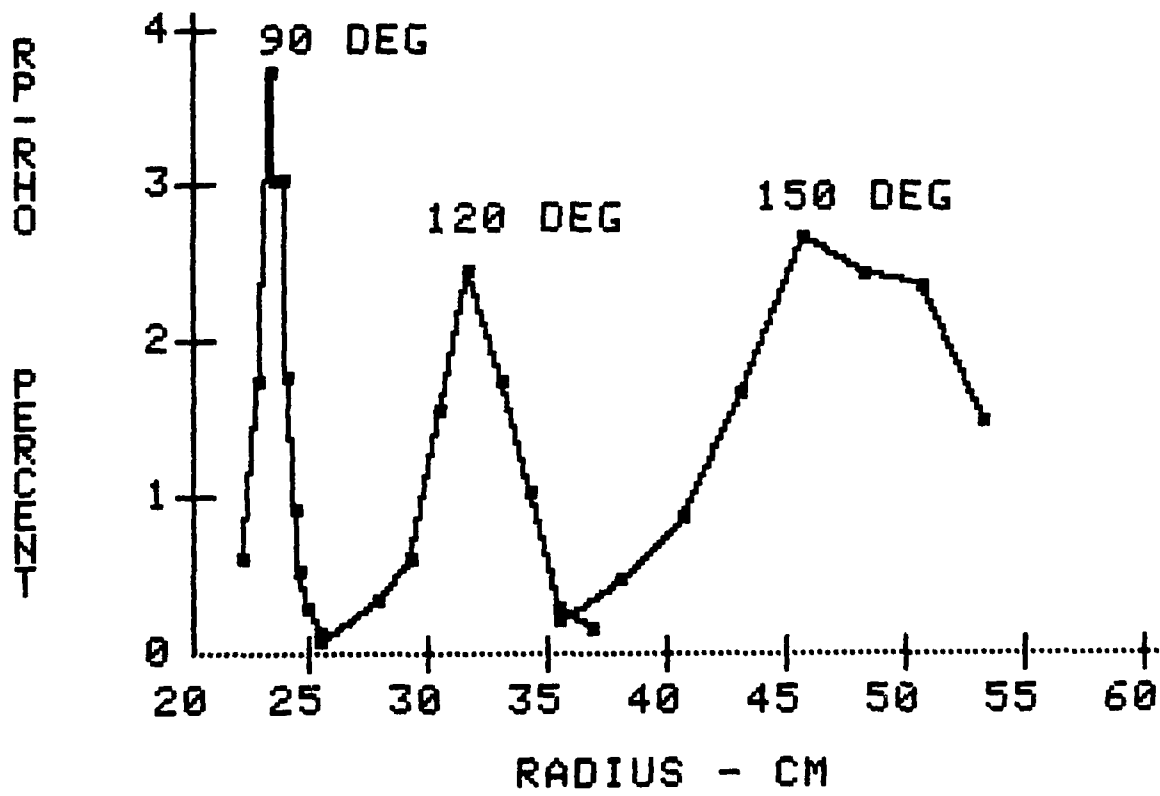


(b) $M = 0.65$

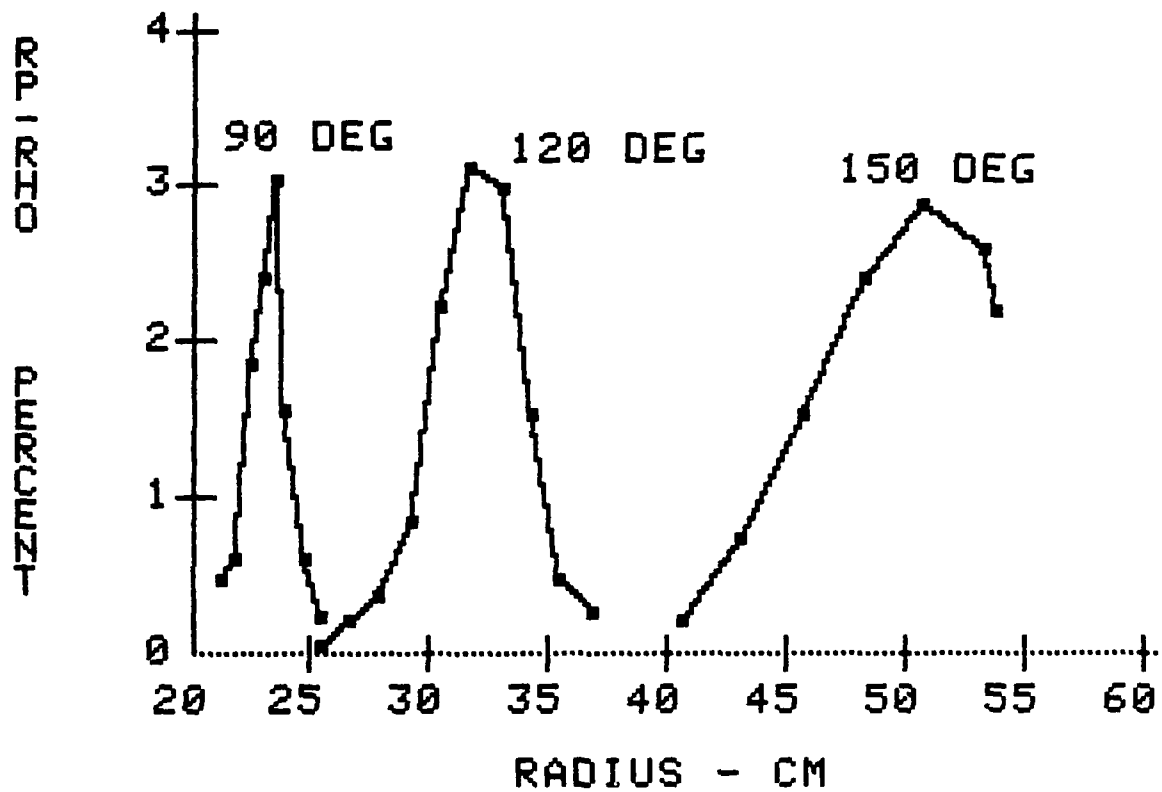
FIGURE 15. (CONTINUED)



(c) $M = 0.75$
FIGURE 15. (CONCLUDED)

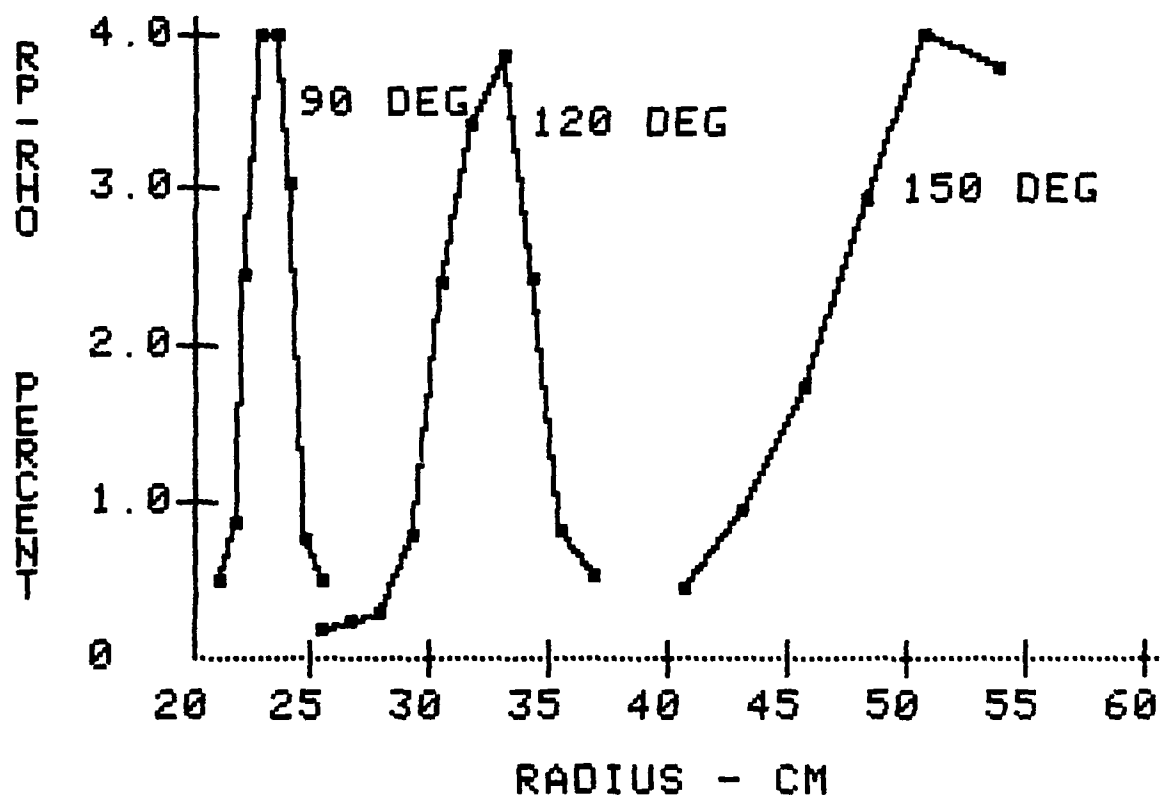


(a) $M = 0.55$
FIGURE 16. DISTRIBUTION OF FLUCTUATING DENSITY, $\langle \rho' \rangle / \bar{\rho}$



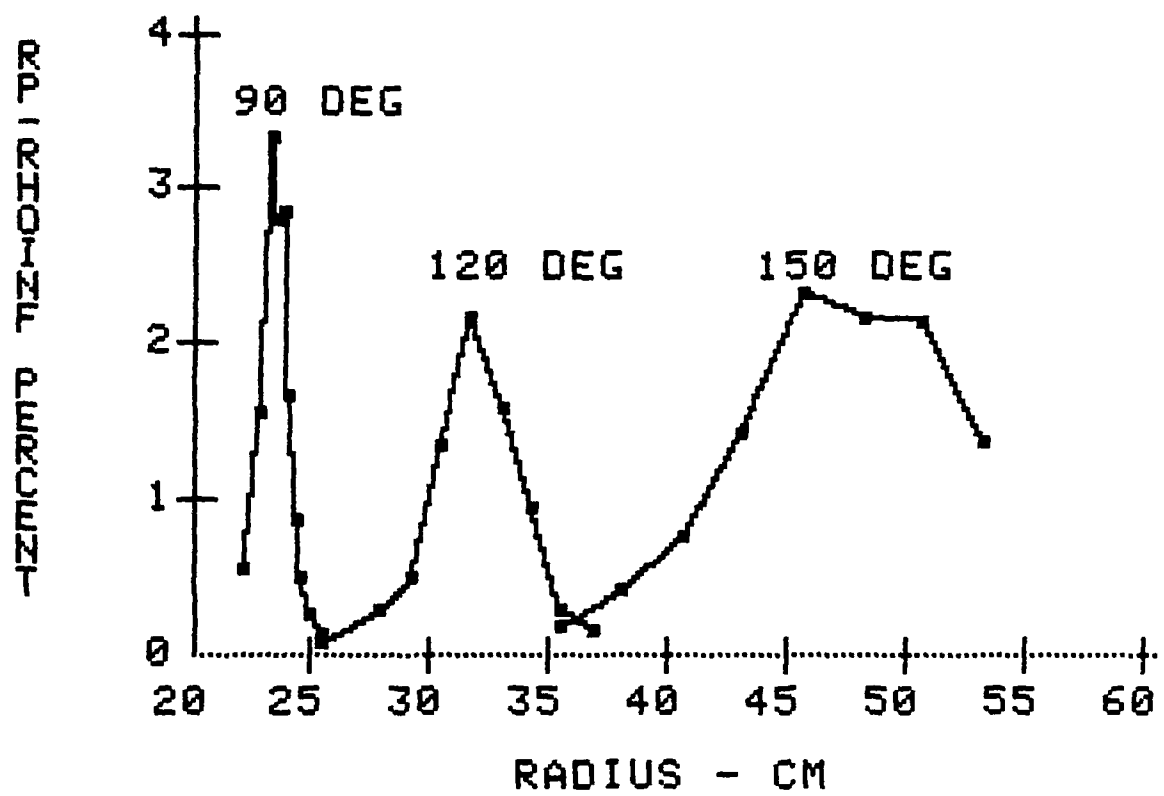
(b) $M = 0.65$

FIGURE 16. (CONTINUED)

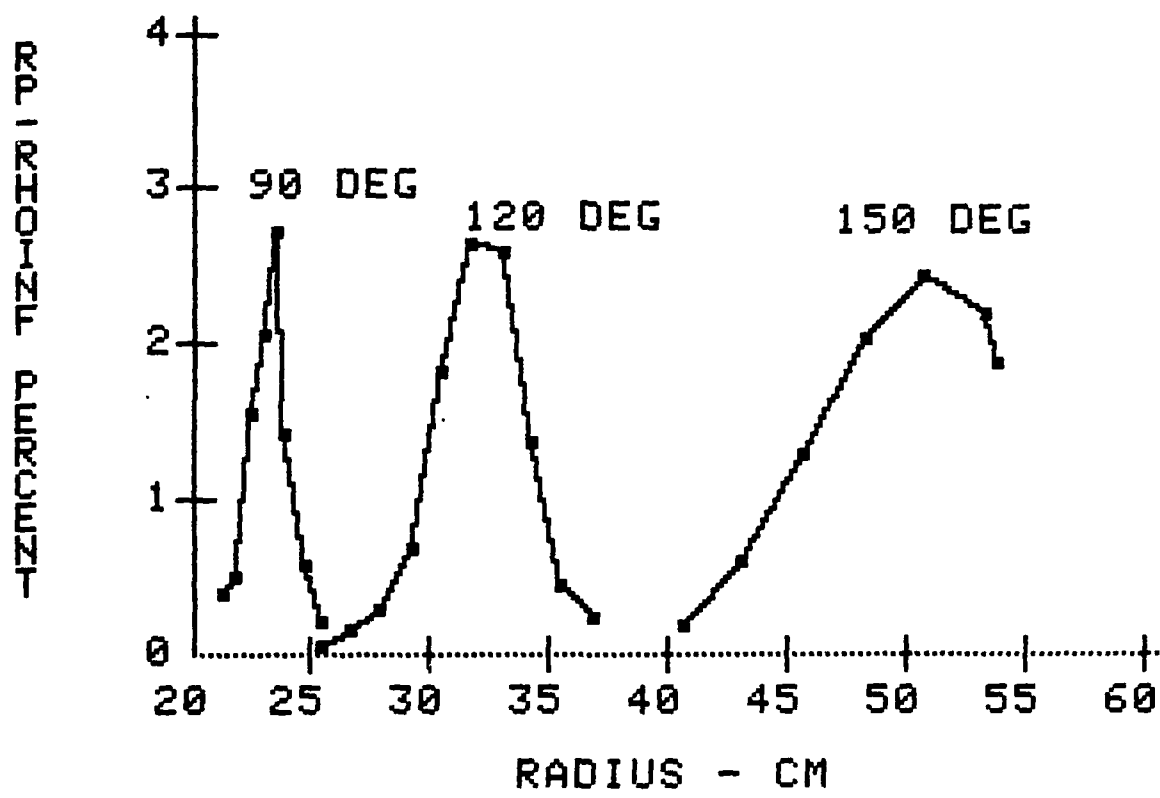


(c) $M = 0.75$

FIGURE 16. (CONCLUDED)

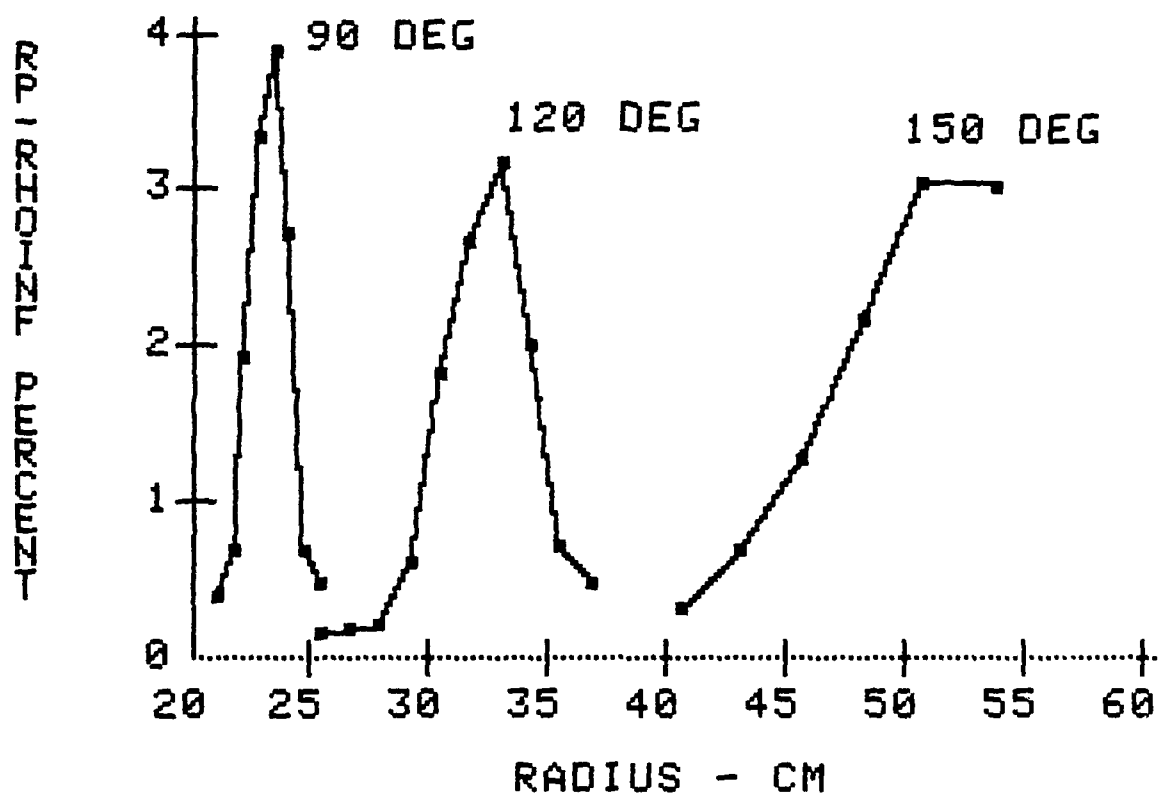


(a) $M = 0.55$
FIGURE 17. DISTRIBUTION OF FLUCTUATING DENSITY, $\langle \rho' \rangle / \rho_\infty$



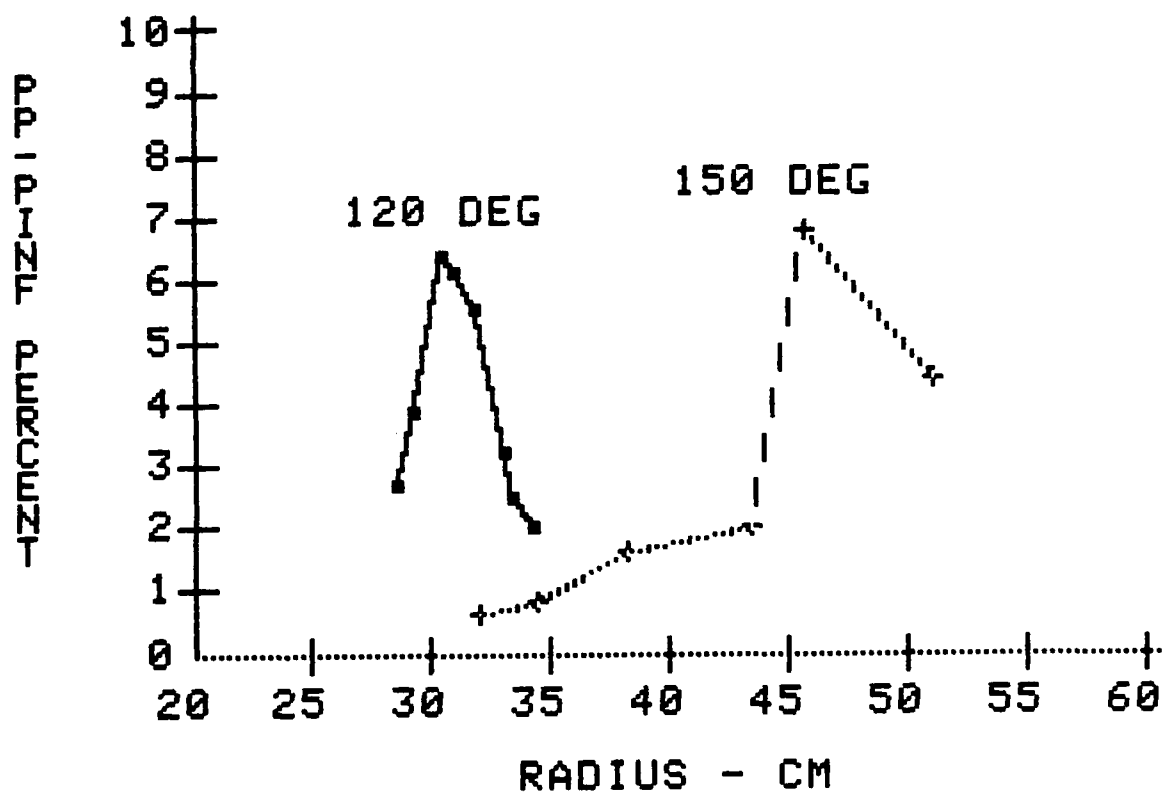
(b) $M = 0.65$

FIGURE 17. (CONTINUED)

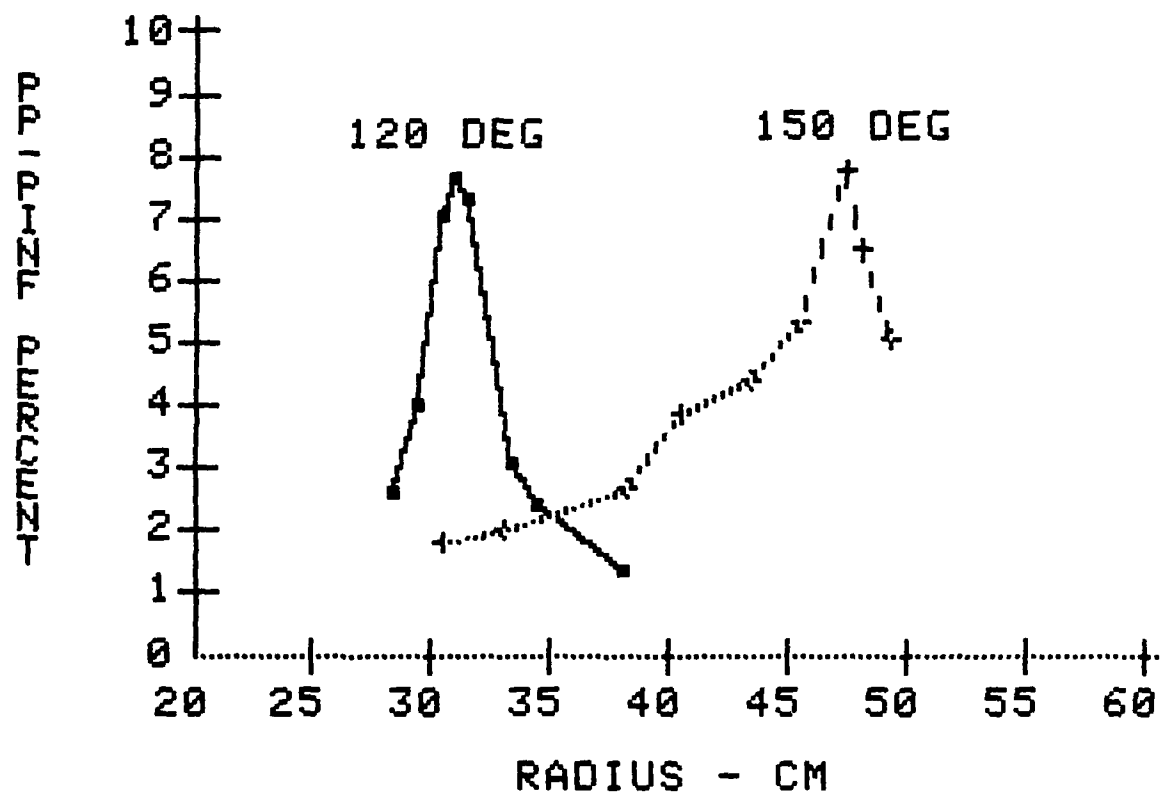


(c) $M = 0.75$

FIGURE 17. (CONCLUDED)

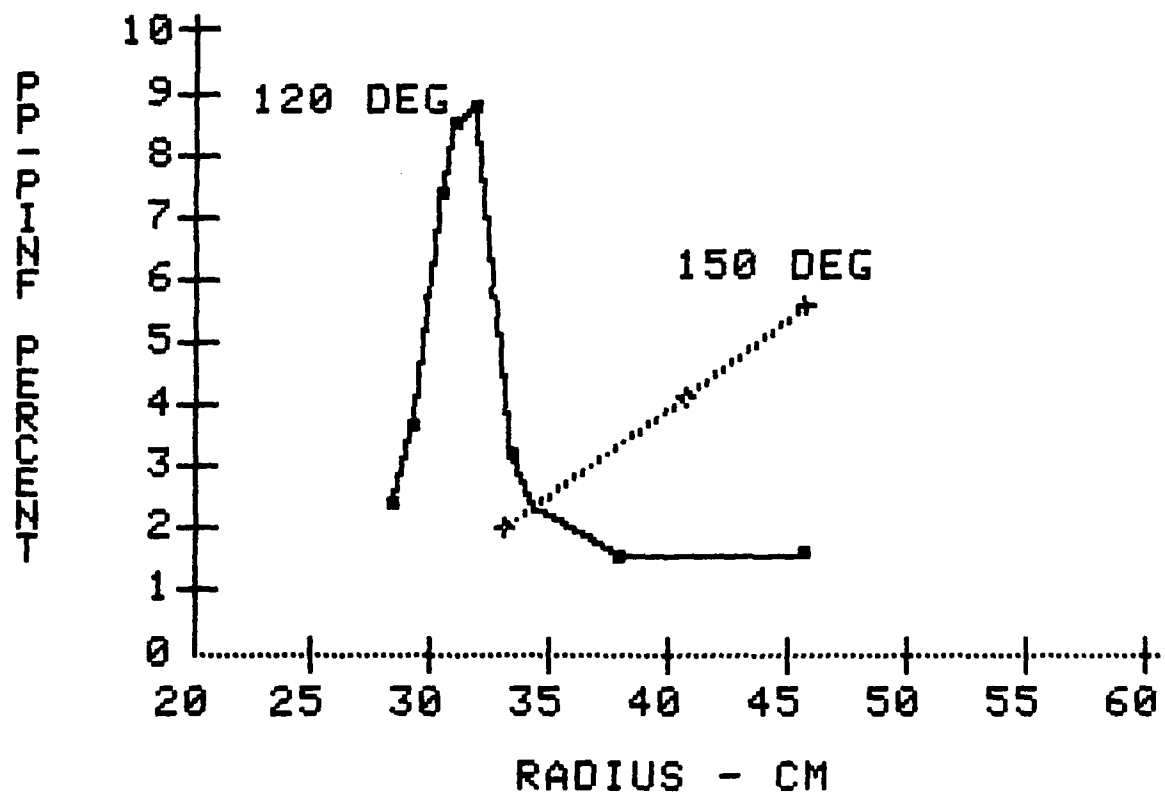


(a) $M = 0.55$
FIGURE 18. DISTRIBUTION OF FLUCTUATING PRESSURE, $\langle p' \rangle / p_\infty$



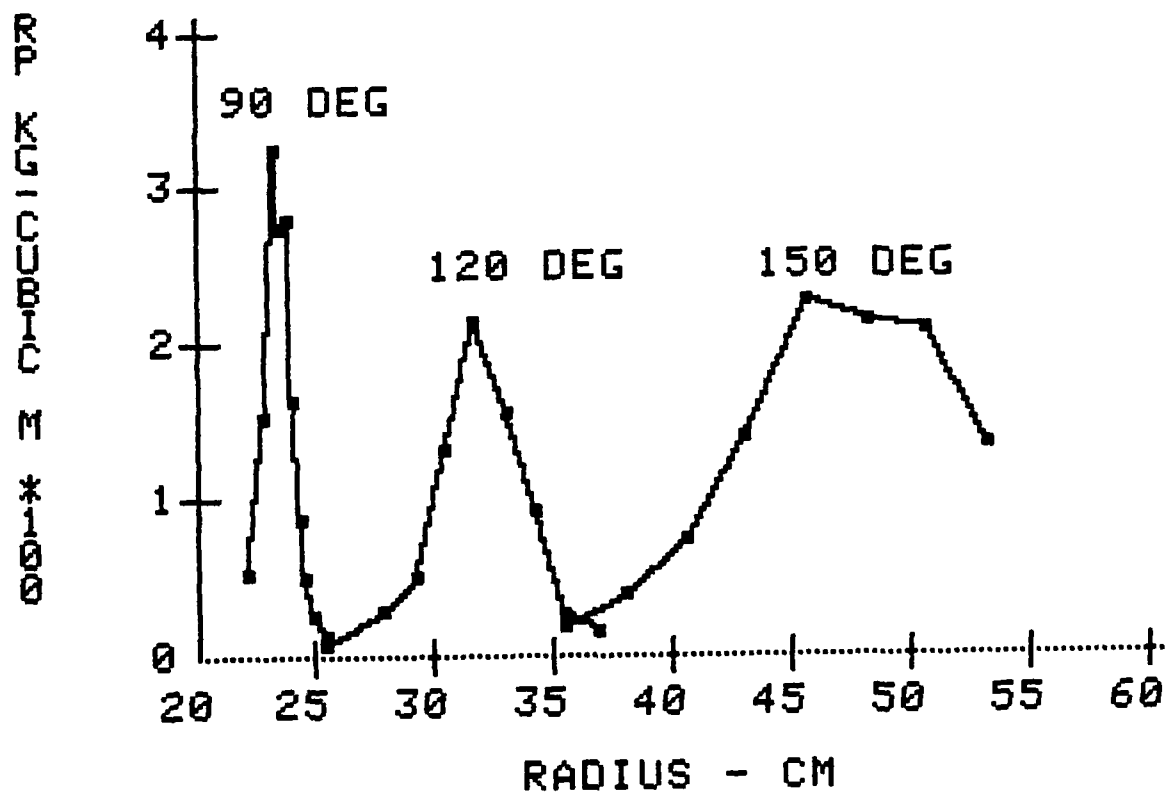
(b) $M = 0.65$

FIGURE 18. (CONTINUED)



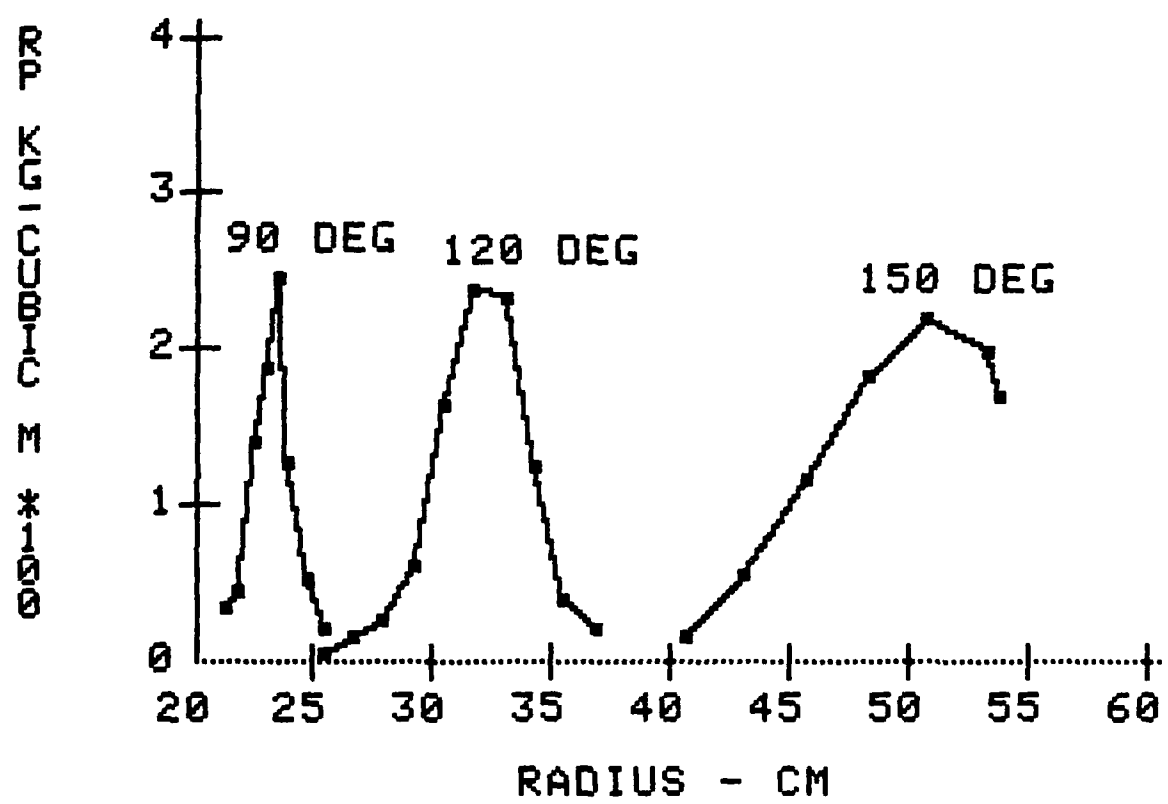
(c) $M = 0.75$

FIGURE 18. (CONCLUDED)

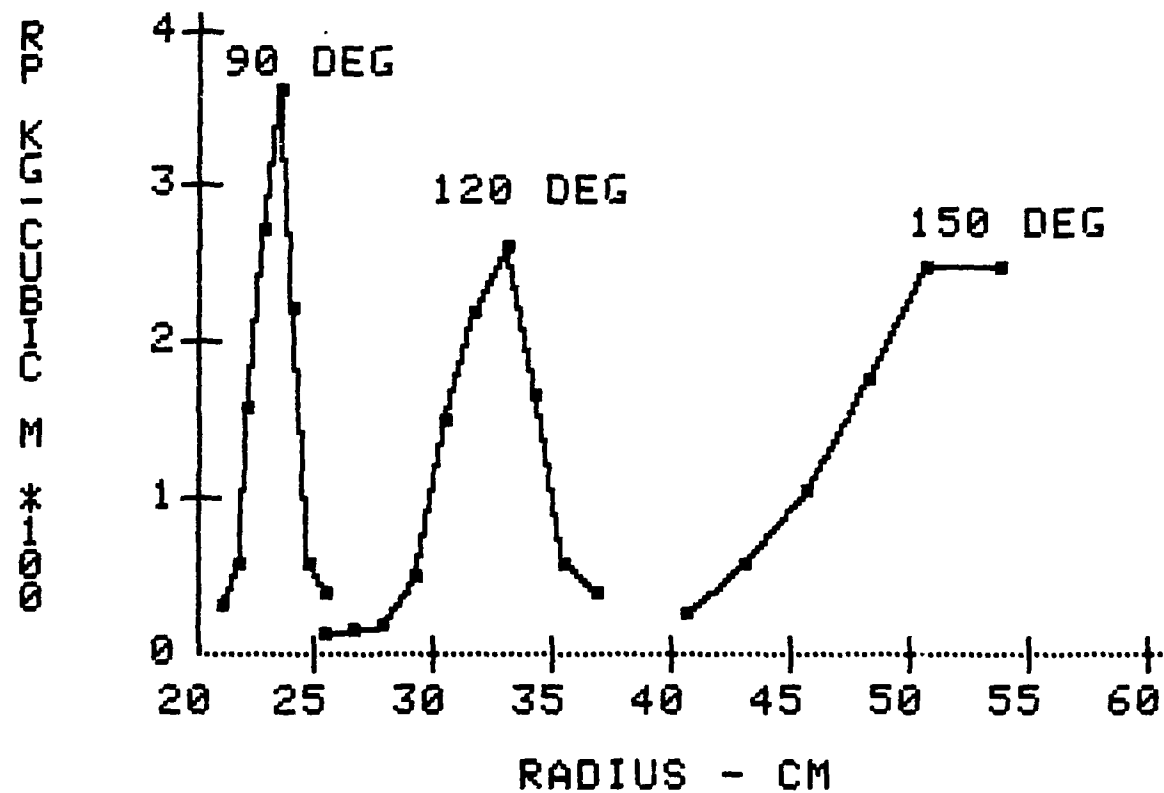


(a) $M = 0.55$

FIGURE 19. DISTRIBUTION OF ABSOLUTE FLUCTUATING DENSITY,
 $\langle \rho' \rangle$, kg/m^3



(b) $M = 0.65$
FIGURE 19. (CONTINUED)



(c) $M = 0.75$
FIGURE 19. (CONCLUDED)

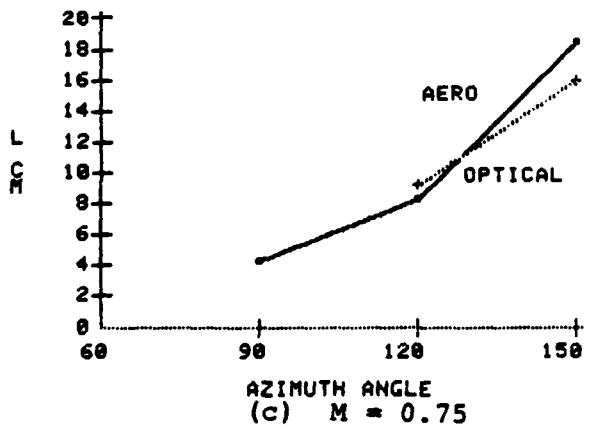
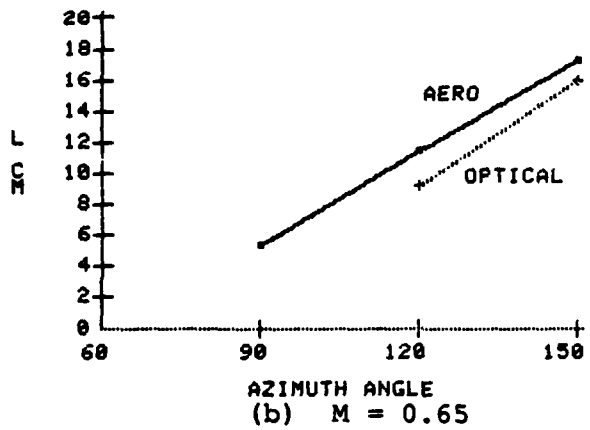
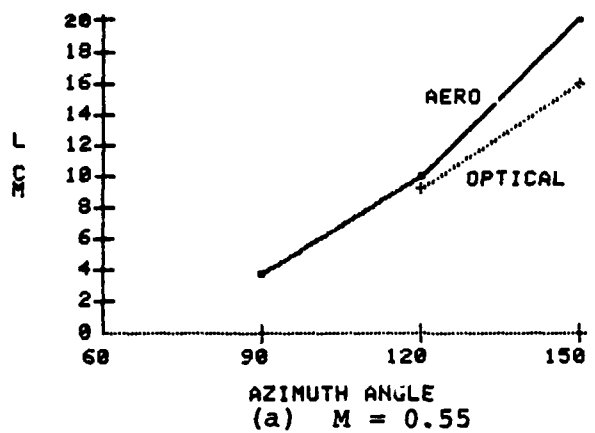


FIGURE 20. VARIATION OF OPTICAL PATH LENGTH, L , WITH AZIMUTH ANGLE

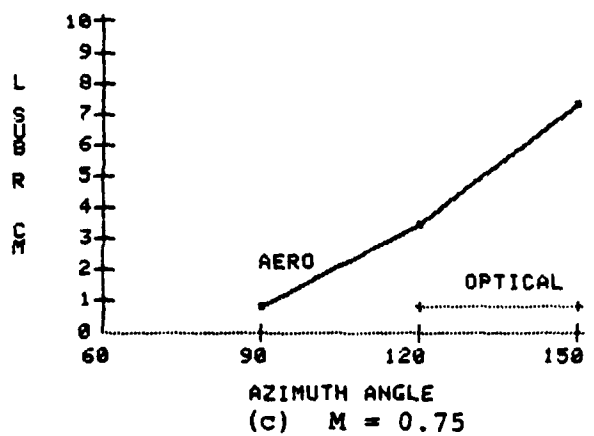
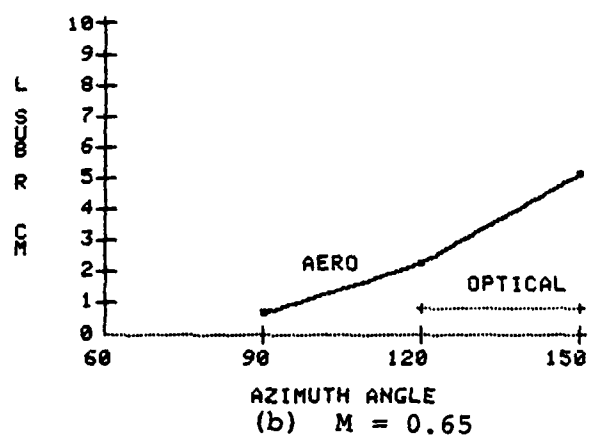
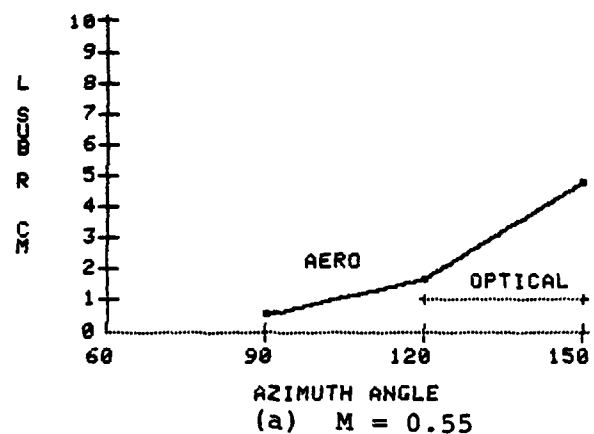


FIGURE 21. VARIATION OF PATH LENGTH SCALE SIZE, ℓ_r , WITH AZIMUTH ANGLE

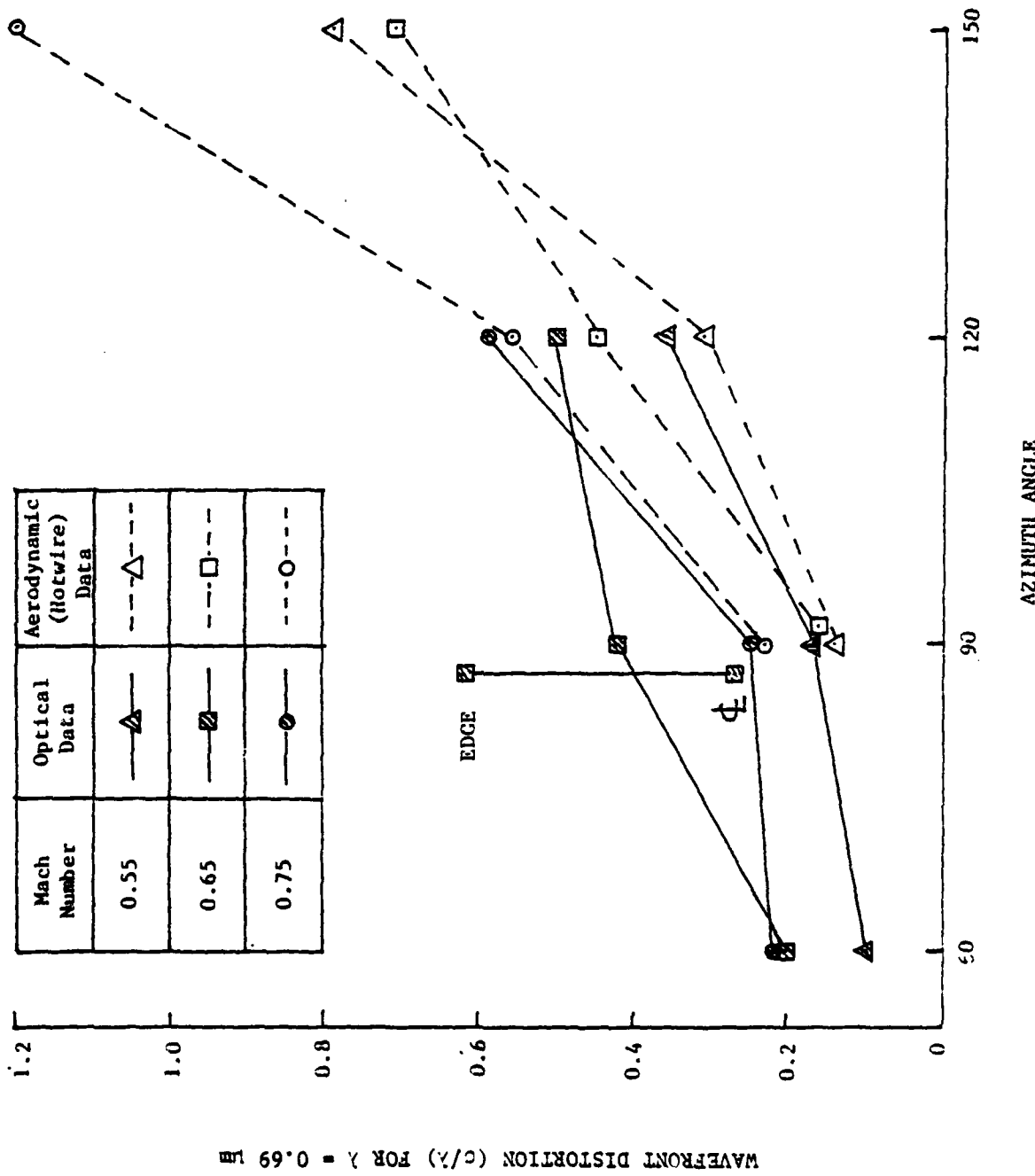


FIGURE 22. COMPARISON OF OPTICALLY AND AERODYNAMICALLY DEDUCED rms WAVEFRONT DISTORTION

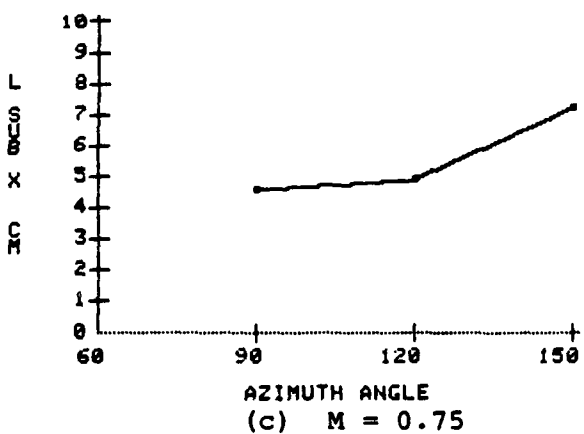
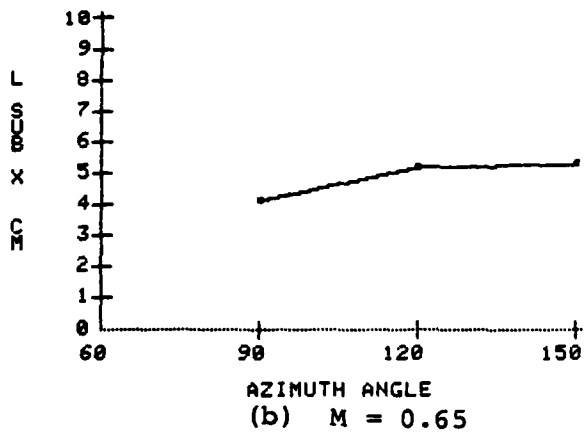
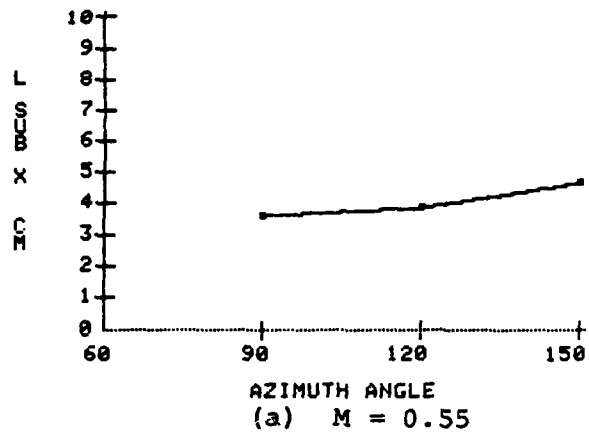
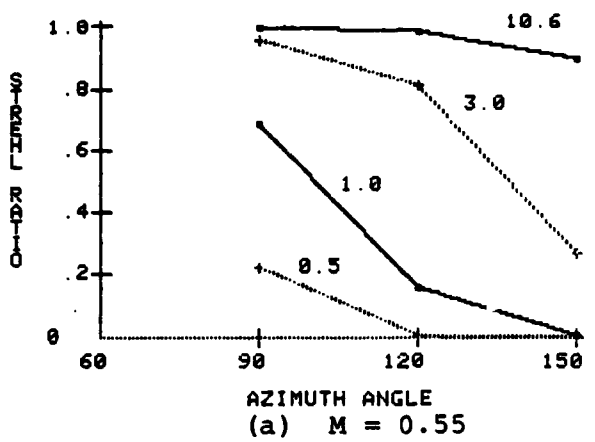
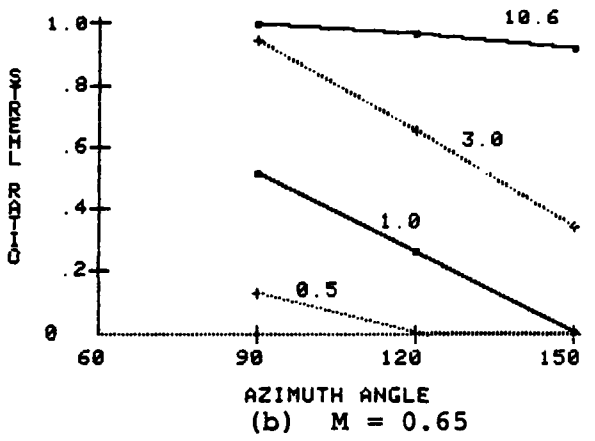


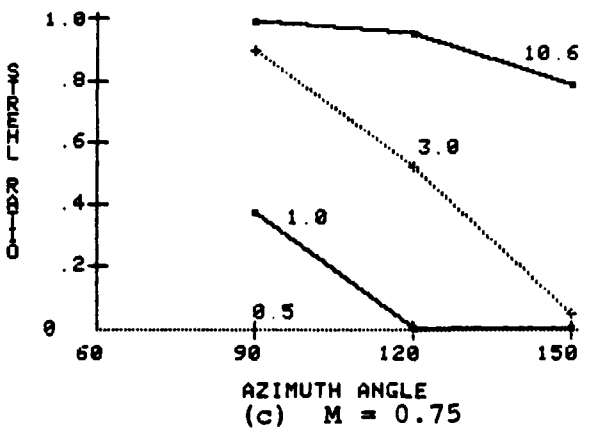
FIGURE 23. VARIATION OF STREAMWISE SCALE SIZE λ_x , WITH AZIMUTH ANGLE



(a) $M = 0.55$



(b) $M = 0.65$



(c) $M = 0.75$

FIGURE 24. VARIATION OF STREHL RATIO WITH AZIMUTH ANGLE

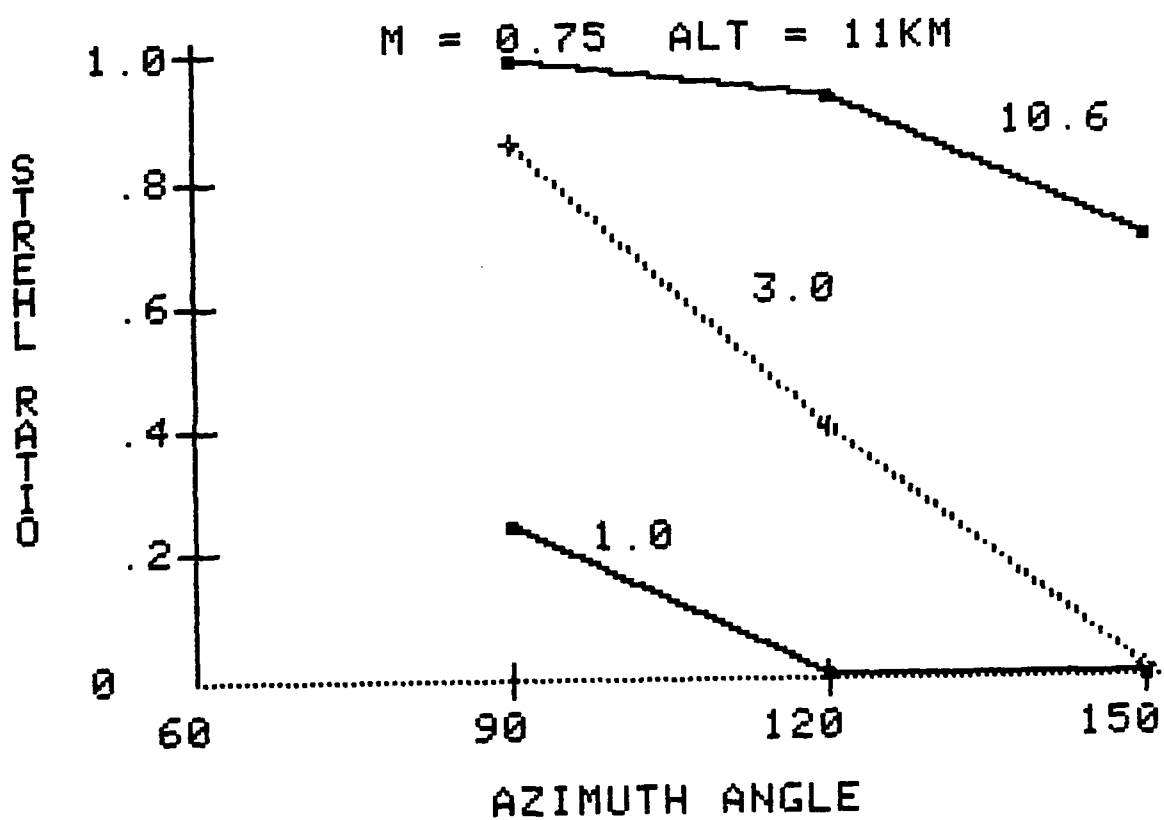


FIGURE 25. STREHL RATIO FOR FULL SCALE FLIGHT CONDITIONS

REFERENCES

1. Gilbert, K.G., Bailey, W.H., and Cook, R.J., "Laser Propagation Through Turbulent Boundary Layers, Shear Layers and Cavity Flows: Wind Tunnel Experiments," Laser Digest - Fall 1977, AFWL TR-78-15, Air Force Weapons Laboratory, Kirtland AFB, NM, April 1978.
2. Gilbert, K.G., "Aircraft Aero-Optical Turbulent Boundary Layer/Shear Measurements," Laser Digest - Fall 1977, AFWL TR-78-15, Air Force Weapons Laboratory, Kirtland AFB, NM, April 1978.
3. Rose, W.C., Measurements of Aerodynamic Parameters Affecting Optical Performance, AFWL TR-78-191, Air Force Weapons Laboratory, Kirtland AFB, NM, April 1979.
4. Buell, D.A., "Overview of 6-x6-Foot Wind Tunnel Aero-Optics Tests," Proceedings of the Aero-Optics Symposium on Electromagnetic Wave Propagation from Aircraft, NASA CP 2121, National Aeronautics and Space Administration, Moffett Field, CA, April 1980.
5. Rose, W.C., Johnson, D.A., and Otten, L.J., III, "Application of Hot-Wire Anemometry and Laser Velocimetry to In-Flight Measurements of Turbulent Flow Properties," AIAA Paper 78-825, San Diego, CA, 1978.
6. Rose, W.C., Optical Effects of Near-Field Turbulence About a Small-Scale Turret Model, AFWL TR-79-129, Air Force Weapons Laboratory, Kirtland AFB, NM, August 1979.
7. Waltrick, R.E. and Van Kuren, J.T., "Flow Visualization Techniques in the Airborne Laser Laboratory Program," Proceedings of the Aero-Optics Symposium on Electromagnetic Wave Propagation from Aircraft, NASA CP 2121, National Aeronautics and Space Administration, Moffett Field, CA, April 1980.
8. Anon., Vol I: Model and Test Information Report; 0.3 Scale APT, Report FZT-203, General Dynamics, Ft. Worth Division, 13 December 1971.
9. Trolinger, J.D.: Laser Instrumentation for Aerodynamics, AGARDograph No. 186, published by NATO/AGARD, March 1974.
10. Trolinger, J.D. and de Jonckheere, R.K.: Aero-Optics IV Holographic Flow Visualization, AFWL TR-79-95, Air Force Weapons Laboratory, Kirtland AFB, NM, September 1979.

AD-A113 910 ROSE ENGINEERING AND RESEARCH INC INCLINE VILLAGE NV F/G 20/6
NEARFIELD AERODYNAMICS AND OPTICAL PROPAGATION CHARACTERISTICS --ETC(U)
FEB 82 W C ROSE, J E CRAIG, K R RAMAN F29601-79-C-0011
AFWL-TR-81-28 NL

UNCLASSIFIED

2 OF 2
AP-A
1-210



END
TRANSMISSION
05-13-82
DTIC

11. Raman, K.R., "Pressure and Temperature Fields Associated with Aero-Optics Tests," Proceedings of the Aero-Optics Symposium on Electromagnetic Wave Propagation from Aircraft, NASA CP 2121, National Aeronautics and Space Administration, Moffett Field, CA, April 1980.
12. Horstman, C.C. and Rose, W.C., "Hot-Wire Anemometry in Transonic Flow," AIAA Journal, Vol 15, March 1977.
13. Hogge, C.B., Strongly Phase-Aberrated Nondiffraction Limited Laser Beams, AFWL TR-75-153, Air Force Weapons Laboratory, Kirtland AFB, NM, January 1976.
14. Gilbert, K.G., "Implications of Recent Aircraft Random Flow Field Experiments for Short Wave-Length Laser Systems," Laser Digest - Summer 1978, AFWL TR-78-174, Air Force Weapons Laboratory, Kirtland AFB, NM, December 1978.

ABBREVIATIONS AND SYMBOLS

I	focal plane peak intensity
L	path length through turbulence
ℓ	correlation length (subscript indicates direction)
k	wave number $2\pi/\lambda$
M	Mach number
n	index of refraction
p	pressure
R_e	Reynolds number
R	radius measured from center of turret
$R(x, \Delta t)$	time correlation function of phase
$R(\Delta x)$	spatial correlation function of phase
T	fluid temperature
t	time
u	fluid velocity
x, y, z	spatial directions
β	Gladstone-Dale constant ($2.3 \cdot 10^{-4} \text{ m}^3/\text{kg}$)
γ	ratio of specific heats (1.4 for air)
$\Delta\phi$	relative phase shift
$\Lambda_{\phi, t}$	integral time scale
λ	wave length of radiation
ϕ	absolute phase shift
ρ	fluid density
σ_{ϕ}^2	optical phase variance
θ	azimuth angle

Subscripts

()'	fluctuation in a quantity
(—)	time average of a quantity
<()>	rms of a quantity
D	based on turret diameter
r	direction along optical axis
t	total or stagnation conditions
x	streamwise direction
y	cross-stream direction
∞	freestream or edge conditions
0	diffraction limited value
$\Delta\phi$	relative phase shift
ϕ	absolute phase shift

Abbreviations

L SUB R	l_r
L SUB X	l_x
PP	$\langle p' \rangle$
PINF	p_∞
RHO	$\bar{\rho}$
RHOINF	ρ_∞
RP	$\langle \rho' \rangle$
UP	$\langle u' \rangle$
UBAR	\bar{u}

